

Beam Geometry Generation: Reverse Beam with Fused Opacity Map

Danh Thanh Phan

School of Science

Thesis submitted for examination for the degree of Master of
Science in Technology.

Helsinki 29.5.2023

Supervisor

Jorma Laaksonen, D.Sc. (Tech.),
Aalto University

Advisor

Victor Pau Bellver López, M.Sc.,
Varian Medical Systems



Aalto University
School of Science

Copyright © 2023 Danh Thanh Phan

Author Danh Thanh Phan

Title Beam Geometry Generation:
Reverse Beam with Fused Opacity Map

Degree programme Master's Programme in Computer, Communication and
Information Sciences

Major Machine Learning, Data Science and Artificial Intelligence
Code of major SCI3044

Supervisor Jorma Laaksonen, D.Sc. (Tech.),
Aalto University

Advisor Victor Pau Bellver López, M.Sc.,
Varian Medical Systems

Date 29.5.2023
Number of pages 74+12
Language English

Abstract

Cancer is hard to cure and radiation therapy is one of the most popular treatment modalities. Even though the benefits of radiation therapy are undeniable, it still has possible side effects. To avoid severe side effects, with clinical evidence, delivering optimal radiation doses to patients is crucial. Intensity-modulated radiation therapy (IMRT) is an advanced radiation therapy technique and will be discussed in this thesis. One important step when creating an IMRT treatment plan is radiation beam geometry generation, which means choosing the number of radiation beams and their directions.

The primary goal of this thesis was to find good gantry angles for IMRT plans by combining computer graphics and machine learning. To aid the plan generation process, a new method called *reverse beam* was introduced in this work. The new solution consists of two stages: angle discovery and angle selection. In the first stage, an algorithm based on the ray casting technique will be used to find all potential angles of the beams. For the second stage, with a predefined beam number, K-means clustering algorithm will be employed to select the gantry angles based on the clusters.

The proposed method was tested against non-small cell lung cancer dataset from The Cancer Imaging Archive. By using IMRT plans with seven equidistant fields with 45° collimator rotations generated by the Ethos therapy system from Varian Medical Systems as a baseline for comparison, the plans generated by the reverse beam method illustrated good performance with the capability of avoiding organs while targeting tumors.

Keywords Beam Geometry, CT Images, Computer Graphics, DICOM, IMRT, K-means Clustering, Machine Learning, Radiation Therapy, Ray Casting, Reverse Beam

Acknowledgements

Finland and Aalto University have given me a great opportunity to become a better version of myself by opening my eyes and changing my mindset in such a profound way. I am grateful for all the new connections I have made, and for all the knowledge that I have gained while pursuing a Master's degree.

I want to express my sincere gratitude to Dr. Jorma Laaksonen, who is my supervisor and academic advisor, for his guidance and thorough feedback on my Master's thesis. I wish to express my appreciation to M.Sc. Victor López, who is my advisor, for his patience and support throughout my work. I would like to acknowledge my colleagues at Varian Medical Systems, especially the Adaptive Treatment Planning team, for their dedication to fighting cancer.

To Lu and Xiu, thank you for being a part of our family and I miss you both.

To Ni, thank you for being my motivation and for growing up with me.

To Ut, Mom and Dad, thank you for your encouragement and your support, even though we are 8.500 km apart.

This work is dedicated to my family.

Helsinki, 29.5.2023

Danh Thanh Phan

Contents

Abstract	3
Acknowledgements	4
Contents	5
Abbreviations and acronyms	7
Operators	8
1 Introduction	9
1.1 Research questions	10
1.2 Structure of the thesis	10
2 Background	12
2.1 Cancer	12
2.1.1 Common types of cancer	12
2.1.2 Why cancer is hard to cure?	14
2.1.3 Treatment modalities	14
2.2 Radiation therapy	15
2.2.1 Information technology in radiation therapy	15
2.2.2 Linear accelerator	16
2.2.3 Types of external radiation therapy	17
2.2.4 Types of radiation beams	18
2.2.5 Definition of target volumes	20
2.2.6 Monitor unit	21
2.2.7 Dose distribution	22
2.2.8 Clinical workflow of radiation therapy	24
2.3 Computer graphics	25
2.3.1 Viewing pipeline	26
2.3.2 Transformations	27
2.3.3 Rendering	29
2.3.4 Ray tracing and ray casting	31
2.4 Machine learning	32
2.4.1 Machine learning types	32
2.4.2 Clustering	34
2.4.3 Clustering distance metrics	35
2.4.4 Clustering evaluation metrics	36
3 Research materials	38
3.1 NSCLC-Radiomics dataset	38
3.1.1 Data description	38
3.1.2 Data processing	39
3.2 Radiotherapy plans and doses dataset	42

3.3	Data analysis	43
3.4	Development setup	46
4	Methods	48
4.1	Existing methods	48
4.2	Reverse beam	48
4.2.1	Angle discovery	49
4.2.2	Angle selection	52
5	Evaluation	54
5.1	Performance	54
5.2	Comparison	55
5.3	Ranking angles	60
5.3.1	Observations	60
5.3.2	Result	62
5.4	Future development	65
6	Conclusions	67
	References	68
A	Angle discovery performance	75
B	Angle discovery result	77

Abbreviations and acronyms

3D-CRT	three-dimensional conformal radiation therapy
AACR	American Association for Cancer Research
ACS	American Cancer Society
API	application programming interface
BNCT	boron neutron capture therapy
CI	conformity index
CNS	central nervous system
CT	computed tomography
CTV	clinical target volume
DICOM	Digital Imaging and Communications in Medicine, the international standard for medical images and related information.
DoF	degree of freedom
GCO	Global Cancer Observatory
GPU	graphics processing unit
GTV	gross tumor volume
IAEA	International Atomic Energy Agency
IMRT	intensity-modulated radiation therapy
ITV	internal target volume
LINAC	linear accelerator
MDP	Markov decision process
MU	monitor unit
NCI	National Cancer Institute
NSCLC	non-small cell lung cancer
OAR	organs at risk
PTV	planning target volume
RMSE	root mean square error
ROI	region of interest
RTDOSE	DICOM radiotherapy dose
RTPLAN	DICOM radiotherapy plan
RTSTRUCT	DICOM radiotherapy structure set
SBRT	stereotactic body radiotherapy
SCLC	small cell lung cancer
SRS	stereotactic radiosurgery
SRT	stereotactic radiation therapy
SSD	source to surface distance
SSE	sum of squared error
TCIA	The Cancer Imaging Archive
VMAT	volumetric modulated arc therapy
WHO	World Health Organization

Operators

$a \cdot b$	dot product of vectors a and b
$\ a\ $	magnitude of a vector a
$d^t(x_1, x_2)$	t -norm distance between x_1 and x_2

1 Introduction

“ Cancer is a leading cause of death worldwide, accounting for nearly 10 million deaths in 2020. ”

World Health Organization [1], Global Cancer Observatory [2]

According to [Global Cancer Observatory](#) (GCO)¹, approximately 20 million cancer incidences were reported in 2020 [2]. With the given statistics, receiving "you have cancer" understandably strikes fear into the hearts of millions of patients around the world. However, the last decade has seen significant advances in the fight against cancer. For example, treating cancer became more precise because cancer treatment changed from the one-size-fits-all approach to personalized medicine based on the detailed genetic information of the patient's specific cancer [3]. As indicated in the Annual Report to the Nation on the Status of Cancer by [National Cancer Institute](#) (NCI)², "from 2015 to 2019, cancer death rates decreased 2.3% per year (on average) for men and 1.9% per year (on average) for women" [4].

Depending on the type and the stage of the cancer, doctors and the patient will make decisions about treatment plans accordingly. The most common cancer treatment modalities are surgery, chemotherapy, and radiation. [American Cancer Society](#) (ACS)³ reported that more than half of cancer patients receive radiotherapy [5]. Even though the benefits of radiation therapy are undeniable, it still has possible side effects, such as slightly raising the risk of getting another cancer. Since the fundamental of radiotherapy is to damage the DNA of cancer cells using radiation, surrounded healthy tissues and organs will be incidentally irradiated as a consequence. Olsson et al. [6] showed the relationships between severe symptoms and dose tolerances from 33 identified studies including 36 to 746 patients per symptom domain. With the clinical evidence, delivering optimal doses to patients is crucial.

With the advances in technology, especially artificial intelligence (AI), there are more and more practical applications in radiotherapy. For example, the deployment of deep-learning-based image segmentation has significantly sped up the tumor contouring process, in which physicians determine and separate cancer tumors from healthy organs. According to [Siemens Healthineers](#), "95% of the contouring results [generated by AI-Rad Companion Organs RT] are clinically usable or require minor edits" [7]. Another example is the utilization of AI for identifying cancer risks in advance. MIT researchers developed a new AI model that can predict whether a person will develop lung cancer in the next year with accurate percentages ranging from 86% to 94% [8].

Because radiation treatment planning is a complex process involving complicated calculations, optimizations, and simulations, there is still room for improvement. Intensity-modulated radiation therapy (IMRT) is an advanced radiation therapy technique and will be discussed in this thesis. One important step when creating an IMRT treatment plan is beam geometry generation, which means choosing the number of radiation beams and their directions. With the inspiration from how ray casting is used in computer

¹<https://gco.iarc.fr/>

²<https://www.cancer.gov/>

³<https://www.cancer.org/>

graphics for rendering and the rapid growth of AI, a new beam geometry generation method is proposed in this thesis with the aim to speed up the process while maintaining the treatment quality.

1.1 Research questions

Even though modern treatment planning systems for radiotherapy are capable of creating a new treatment plan within minutes, generating a high-quality one with acceptable dose distribution is still a time-consuming task. Dose objectives for the target and the organs at risk (OAR) need to be fine-tuned manually by medical physicists and medical dosimetrists, and this process needs to be repeated until all clinical goals are reached. Additionally, the plan quality is also affected by multiple elements, such as the experience of the planner, the allotted time for plan generation, or even the guidelines of the medical department.

A new solution, which is called **reverse beam**, is proposed and studied in this thesis to aid the workflow. The method consists of two stages: angle discovery and angle selection. In the first stage, an algorithm based on the ray casting technique will be used to find all potential angles of the beams (fields). For the second stage, with a predefined beam number, K-means clustering algorithm will be employed to aid the users in selecting the gantry angles based on the clusters.

By using the proposed method to generate IMRT plans targeting lung cancer with data from The Cancer Imaging Archive (TCIA)⁴, the thesis aims to answer the fundamental quantitative question "Can the advanced beam geometry generation algorithm still be improved" via the following observations:

1. How well does the proposed method perform, in terms of performance and quality?
2. How do the new plans compare to the ones with equidistant fields?
3. Is there an IMRT plan that has fewer beams than the given one, but is still capable of achieving the same clinical goals?

1.2 Structure of the thesis

The thesis consists of six chapters. The first chapter, which you are reading, states the motivation and the story behind it. Chapter 2 introduces background information related to cancer, computer graphic, and machine learning. It is worth mentioning that this chapter will not be able to cover all aspects of the given topics. However, the provided knowledge will be sufficient to act as the foundation to build up the proposed solution. Chapter 3 describes the TCIA dataset, how to process it, and how it was used to generate the radiotherapy plans and doses dataset. The environment setups for development are also defined in the same chapter. In Chapter 4, the existing methods are described and the new solution is delivered. The performance and quality are revealed in Chapter 5 by comparing and contrasting with plans generated by Ethos⁵ therapy system. In

⁴<https://www.cancerimagingarchive.net/>

⁵Varian Medical Systems, Palo Alto, CA

addition, this chapter also discusses how the proposed method can be further improved and suggests ideas for future work. Finally, Chapter 6 concludes the thesis.

2 Background

All key concepts of the work will be provided in this chapter. First of all, a brief introduction to cancer and its types will be given to explain why cancer is so hard to cure. Then, radiation therapy will be described. How information technology has been used in radiation therapy will be discussed as this work follows the standards and conventions. Furthermore, an overview of computer graphics and machine learning will be presented, as they are the foundation stone of this thesis. It is worth mentioning that the theory will be provided on "just enough" basics, since there are well-written books that covered the mentioned topics in detail.

2.1 Cancer

“ Cancer is a large group of diseases that can start in almost any organ or tissue of the body when abnormal cells grow uncontrollably, go beyond their usual boundaries to invade adjoining parts of the body, and/or spread to other organs. ”

World Health Organization [1]

Cancer is classified as a genetic disease [9]. Genes are sections of DNA that carry instructions to make a protein or several proteins. The basic building blocks of the human body are cells and each cell has a copy of our genes. Normally, if faults exist in genes, they will be repaired by cells and when the damage is severe, the cell will self-destruct or be killed by the immune system for being recognized as abnormal. Thanks to this mechanism, the human body is protected from cancer. However, the mutation of important genes sometimes causes a cell to no longer follow the instructions. The mentioned cell, which then starts to multiply out of control, will not repair itself properly nor die when it should. This can lead to cancer.

Cancer-related genetic changes can occur due to multiple reasons. For example, a random DNA mistake happens as our cells multiply, or carcinogens in the environment alternate our DNA. Additionally, [World Health Organization](https://www.who.int/) (WHO)⁶ states that "around one-third of deaths from cancer are due to tobacco use, high body mass index, alcohol consumption, low fruit and vegetable intake, and lack of physical activity" [1].

The amount and spread of cancer in a patient's body are described by using the TNM staging system. According to NCI, the TNM staging system is defined as follows: "The T refers to the size and extent of the main (primary) tumor", "the N refers to the number of nearby lymph nodes that have cancer", and "the M refers to whether the cancer has metastasized" [10].

2.1.1 Common types of cancer

As cancer incidences vary widely by geography, lifestyle, and other external factors, cancer statistics on a global scale can be provided to give an overview of common types of cancers.

⁶<https://www.who.int/>

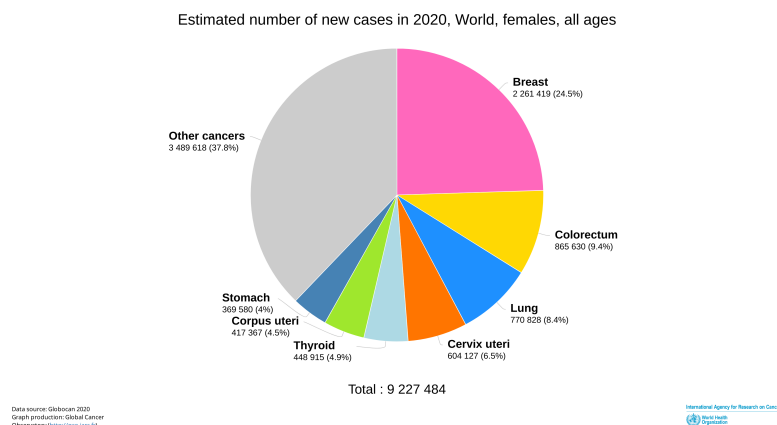


Figure 1: Estimated number of new cancer cases in 2020. Population: World. Sex: females. Age groups: all ages. [2]

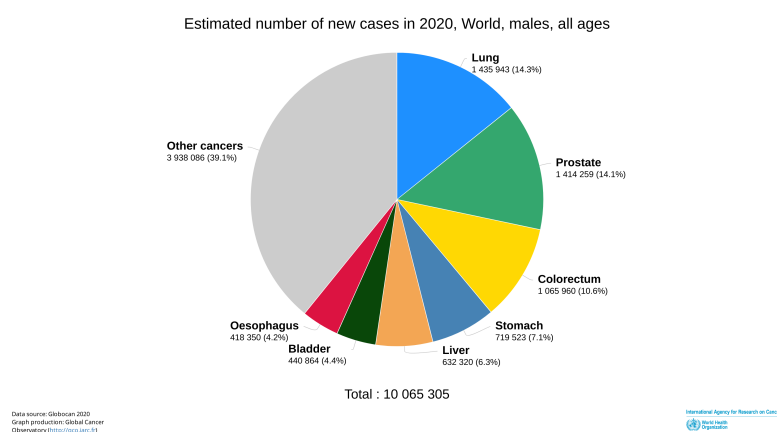


Figure 2: Estimated number of new cancer cases in 2020. Population: World. Sex: males. Age groups: all ages. [2]

According to GCO [2]:

1. Breast cancer is the most common cancer in women worldwide. As shown in Figure 1, there were more than 2.3 million new cases of breast cancer in 2020.
2. Lung cancer is the most common cancer in men worldwide. Figure 1 and Figure 2 reveal that in 2020, there were around 2.2 million new cases of lung cancer.
3. Prostate cancer used to be the leading cancer diagnosis among men worldwide. As seen in Figure 2, there were approximately 1.4 million new cases of prostate cancer in 2020.

2.1.2 Why cancer is hard to cure?

Per [American Association for Cancer Research](https://www.aacr.org/) (AACR)⁷ and NCI, cancer is not a single disease, but a group of more than 100 distinct ones, which are classified based on the type of cell that they start in [11] [12]:

1. **Carcinomas** are the most common type of cancer [12]. They occur on the skin or tissues that line internal organs [11].
2. **Sarcomas** are cancers that occur in the bone, cartilage, fat, muscle, blood vessels, or other connective or supportive tissue [11].
3. **Leukemias** are cancers that occur in the cells of the blood and bone marrow [11].
4. **Lymphomas** are cancers that occur in the cells of the immune system and typically appear within the lymphatic system [11].
5. **Central nervous system (CNS) cancers** are cancers that occur in the cells of the brain and spinal cord [11].

As cancers originate from a build-up of cell mutations, two people with the same broad type of cancer might have different accumulated mutations. Hence, a drug that works for one patient might have absolutely no effect on another. Moreover, there is a commonly known phenomenon called drug resistance, which describes the situation when cancer cells contain molecular changes that make themselves insensitive to a particular drug. It means a cancer patient may have success with a treatment for some time, but ultimately finds out the course just stops working.

2.1.3 Treatment modalities

There are different types of cancer treatment and some common types of cancer mutation respond to a certain treatment. According to ACS, the most common treatment options are [13]:

1. **Surgery** is the earliest form of cancer treatment and originates with attempts at curative resections. Bowser and Waxman state that there are six main roles of surgical oncology: "cancer prevention, cancer diagnosis and staging, treating cancer, management of oncological emergencies, palliation of cancer symptoms, and surgical reconstruction following cancer therapy" [14].
2. **Chemotherapy or chemo** uses drugs to destroy cancer cells. There are three main roles of chemotherapy in cancer treatment: cure, control, and palliation. Chemo is a systemic treatment because the drugs travel throughout the body, in contrast to local treatments such as surgery and radiation therapy which affect one part of the body [15].

⁷<https://www.aacr.org/>

3. **Hormone therapy** or **endocrine therapy** uses hormones to treat cancer. Some cancers depend on hormones to grow and by blocking or altering hormones, the growth of the cancer can be slowed or stopped. As stated by ACS, "hormone therapy is mostly used to treat certain kinds of breast cancer and prostate cancer" [16].
4. **Radiation therapy** or **radiotherapy**, which is written in more detail in Section 2.2, uses different types of radiation beams to destroy cancer DNA.

A suitable treatment course will be chosen depending on several factors, such as the type of cancer, its stage, its location, as well as the patient's overall health and medical records. According to NCI: "Some people with cancer will have only one treatment. But most people have a combination of treatments, such as surgery with chemotherapy and radiation therapy" [17].

2.2 Radiation therapy

“ Radiotherapy remains the most effective non-surgical treatment in the management of malignant disease. ”

Peter Hoskin [18]

Radiation therapy is defined as a treatment using "high doses of radiation" to "kill cancer cells or slow their growth by damaging their DNA" [19]. When the DNA of the cancer cells is damaged beyond repair, the cells will stop dividing and eventually die. Then, they will be broken down and removed by the body. Unfortunately, due to the radiation therapy mechanism, patients might face side effects, including fatigue, skin reactions, nausea, and hair loss, among others. However, the symptoms can vary depending on the type and intensity of the treatment, and many can be reduced with medication or supportive care.

Radiation therapy is a local treatment [19], which means it treats only the targeted part of the body that contains the tumor. There are two main types of radiation therapy: internal and external [19]. Internal radiation therapy is a treatment in which a source of radiation, such as radioactive metal or capsules, is put inside the body. With external radiation therapy, a treatment unit is used to aim beams of radiation at the tumor.

2.2.1 Information technology in radiation therapy

“ Modern radiotherapy departments cannot function without IT support. ”

Niall MacDougall and Andrew Morgan [18]

Information technology plays a critical role in radiation therapy. It is used to manage patient records, imaging data, and treatment plans, as well as to facilitate communication and collaboration between radiation therapy team members.

Digital Imaging and Communication in Medicine (DICOM)⁸ is the international standard for the management and transmission of medical data. By using the DICOM

⁸<https://www.dicomstandard.org/>

standard, medical equipment from different manufacturers is capable of sending and receiving data without the need for data conversion. DICOM files can contain a variety of data, such as patient demographic information, imaging modality, and image data.

A treatment planning system is used to develop treatment plans. The software allows treatment plans to be optimized and ensures the radiation dose is delivered accurately and precisely. Additionally, it is capable of running a treatment delivery simulation to guarantee that a collision between the patient and the treatment unit does not happen.

2.2.2 Linear accelerator

To deliver radiation doses in external radiation therapy, a **linear accelerator (LINAC)** is widely used. As seen in Figure 3, it consists of a large metal structure that houses the radiation source and a treatment couch.

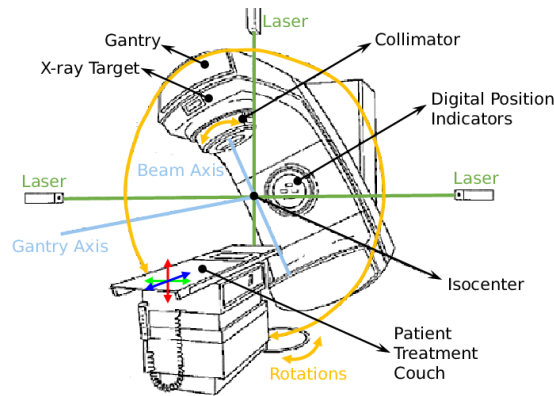


Figure 3: Schematic depiction of a LINAC used in external beam radiation therapy. [20]

The radiation source is produced by accelerating electrons through a waveguide and directing them toward a heavy metal target, such as tungsten. After that, the collisions will emit high-energy X-rays or electrons, which are then directed at the tumor.

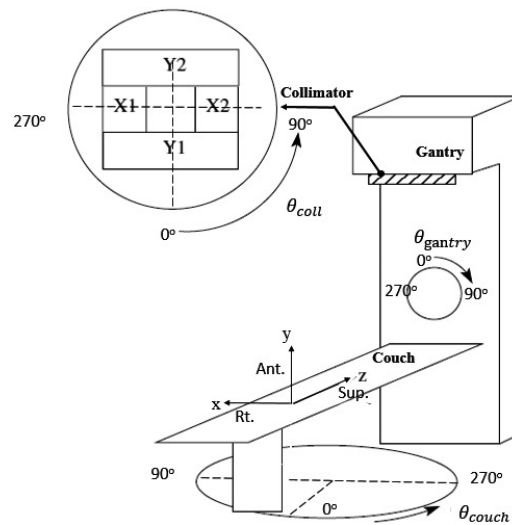


Figure 4: LINAC coordinate systems (X, Y, Z) and the available movements. [21]

The coordinate systems illustrated in Figure 4 will be used throughout the thesis work unless stated otherwise. The collimator, gantry, and couch are capable of rotating and moving independently around the isocenter. The versatility in the movements of these treatment units allows them to deliver various forms of external radiation therapy.

2.2.3 Types of external radiation therapy

External radiation therapy is commonly used to treat solid tumors, such as cancers of the prostate, breast, lung, head, and neck. It can also be used to alleviate symptoms such as pain or bleeding caused by tumors that cannot be removed surgically. There are many different types of external radiotherapy, including but not limited to [22]:

1. **Three-dimensional conformal radiation therapy (3D-CRT)** constructs the detailed three-dimensional models of the patient's anatomy from computed tomography (CT) or magnetic resonance imaging (MRI) scans [22]. By using the models to aim the beams, high doses can safely be used while lowering the risk of side effects as damage to healthy tissue is avoided.
2. **Stereotactic radiation therapy (SRT)** is capable of delivering a large and precise dose to a small tumor area. The patient must remain completely still with the help of shells or molds so the treatment can be accurate as possible [22]. Different terms for stereotactic radiotherapy are used depending on the treatment site. If it is the brain, **stereotactic radiosurgery (SRS)** is used, and **stereotactic body radiotherapy (SBRT)** for the body.
3. **Intensity-modulated radiation therapy (IMRT)** delivers a highly precise dose of radiation to the tumor by using multiple radiation beams from multiple distinct angles. Not only the shape but also the intensity of the radiation beams can be adjusted during the treatment. While 3D-CRT uses the same intensity for each beam, the dynamic intensity of IMRT beams helps it avoid healthy tissue better.
4. **Volumetric modulated arc therapy (VMAT)** delivers radiation in continuous arcs while simultaneously adjusting the intensity and the shape of the beam. This allows VMAT to deliver radiation more quickly than IMRT and reduces the overall treatment time for the patient. Hence, it is used for patients who are unable to lie still for long periods of time.

Figure 5 illustrates the beam geometry of different IMRT and VMAT plans, which were generated by using Ethos therapy system, for the same patient with the same clinical goals. The thick pink plane is the couch and the green objects are the lungs. The gantry positions for IMRT plans are represented by the yellow squares and the gantry movement for VMAT plans are illustrated by the red circles. As the tumor totally locates in the left lung, lateral and half-arc plans are also valid options where the healthy right lung is not exposed to radiation. Besides multiple types of external radiotherapy, there are different types of radiation beams.

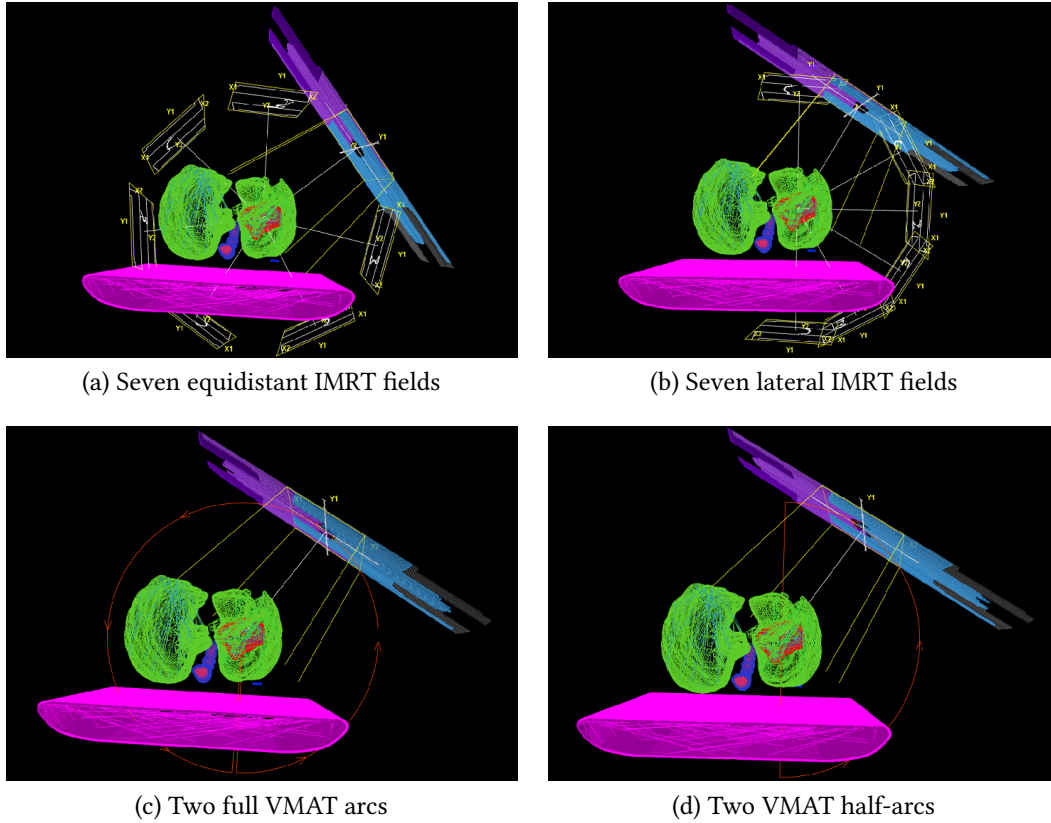


Figure 5: Beam geometry of different IMRT and VMAT plans.

2.2.4 Types of radiation beams

The radiation beams of external radiation therapy come from three types of particles: photons, protons, and electrons [23]. The latter ones, protons, and electrons, together with neutrons, are the three basic particles that construct atoms. Hence, it is understandable to question why neutrons are not commonly used in radiation therapy. This will be explained shortly. As carbon ion is used in radiotherapy, the structure of a carbon atom is illustrated in Figure 6.

Photons are fundamental particles representing a quantum of light or other electromagnetic radiation. The NCI states that photon beams are available on most radiation therapy machines and are employed to treat tumors located deep inside the body [23]. However, this type of beam scatters radiation along the path while traveling through the body. Hence, it is important to target the photon beam carefully to minimize radiation exposure to healthy tissue while maximizing its effectiveness.

Protons are positively charged particles. Similar to photon beams, proton beams are also utilized to treat tumors deep in the body. Unlike photon beams, proton beams do not scatter radiation on the path and they will stop once they reach the tumor [23]. Therefore, proton beams are useful for treating tumors that are located near critical organs, such as the brain or the spinal cord. However, due to the high cost and the size of the treatment unit, the use of proton beams is limited.

Electrons are negatively charged particles. In contrast to photon beams and proton beams, electron beams have a shallow depth of penetration. As they cannot travel far through body tissues, they are used to treat superficial tumors [23].

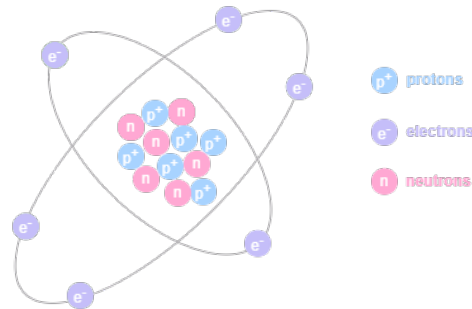


Figure 6: An illustration of the structure of carbon-12 ($^{12}_6\text{C}$).

Neutron beams have been used in the past. Due to unacceptable and unexpected side effects discovered in clinical trials in the 1970s and 1980s, they fell out of favor. One main side effect is a higher risk of radiation-induced secondary cancers in comparison to other types of radiation therapy. This risk is due to the high linear energy transfer radiation from neutrons, which potentially causes complex and dangerous DNA damage. However, in 2021, according to [Physics World](#), boron neutron capture therapy (BNCT) "has shown significant promise in clinical trials for the treatment of malignant brain tumours and locally recurrent head-and-neck cancers – complex indications that are difficult to address using conventional radiotherapy techniques" [24].

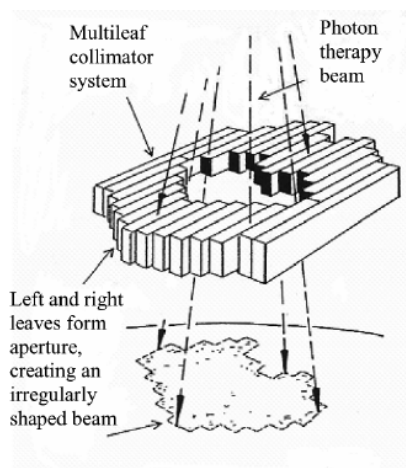


Figure 7: Multileaf collimator system shapes the radiation field to deliver a more precise radiation dose. [25]

The size of the radiation beam can be controlled by using a device called a **beam collimator**, which is constructed of depleted uranium, lead, or tungsten. As seen in Figure 3, it is mounted to the gantry and acts as the last contact point before the beam

leaves the LINAC head. Modern LINACs often have multileaf collimator (MLC), which is made up of several individual metal leaves that can move independently as illustrated in Figure 7. This enables even more precise radiation therapy delivery and better control over the size and shape of the radiation field. As the main goal of the treatment plans is to efficiently eliminate tumors, defining and contouring target volumes that will receive radiation beams is a critical step.

2.2.5 Definition of target volumes

There are several target volume definitions defined by International Commission on Radiation Units and Measurements (ICRU)⁹. They are introduced by [International Atomic Energy Agency](https://www.iaea.org/) (IAEA)¹⁰ in [26] according to Figure 8 as:

1. **Gross tumor volume (GTV)** is the volume that can be seen by the eyes either on the patient or with the help of imaging. This volume follows strictly what is actually seen without adding any margin for possible extension [26].
2. **Clinical target volume (CTV)** is a tissue volume that contains a GTV and/or subclinical microscopic malignant disease, which has to be eliminated [26].
3. **Internal target volume (ITV)** is obtained by adding an internal margin to the CTV. The margin accounts for the variation of position, volume, and shape of CTV during a multifraction treatment [26].
4. **Planning target volume (PTV)** is ITV including geometric uncertainties in daily set-up and machine tolerances [26].
5. **Treated volume** is the region receiving the prescribed dose. In an ideal situation, it would perfectly fit with the PTV. However, it is not uncommon that the prescribed dose to the PTV is actually delivered to a larger volume, especially when the PTV is not a simple geometric figure, such as concave or asymmetrical [26].
6. **Irradiated volume** is the region around the treatment volume, which receives lower doses, but still a significant amount of radiation energy [26].

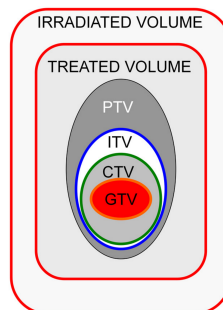


Figure 8: Various target volume definitions from ICRU 50/62/83. [26]

⁹<https://www.icru.org/>

¹⁰<https://www.iaea.org/>

As shown in Figure 3, there is a small dot called **isocenter**, in which the gantry and couch rotate around. This is the point where the radiation beam is most precisely aimed and where the maximum radiation dose is intended to be delivered. Therefore, the isocenter is placed inside the treatment volume and usually overlaps the center of mass of the tumor.

Furthermore, the organ at risk (OAR) is a critical concept that is used throughout the world in daily radiotherapy practice. OARs are normal organs in the body that are close to the target area and are at risk of being damaged by radiation. OARs can vary depending on the location of the tumor, such as the lungs, heart, spinal cord, bladder, and rectum. Damaging OARs during radiation therapy can result in serious side effects and long-term health complications for the patient. Therefore, it is essential to minimize the radiation dose to these normal tissues while ensuring that the tumor receives a sufficient dose to achieve optimal treatment outcomes. This can be achieved through careful treatment planning that takes into account the location of the tumor, the radiation dose needed to treat it, and the proximity of OARs to the tumor.

2.2.6 Monitor unit

Before diving into the monitor unit (MU), the radiation dose should be explained first. According to [Sibtain et al.](#), the dose is defined as "the energy absorbed by a fixed amount of material" [18]. Its unit is Gray (Gy) and $1\text{Gy} = \frac{1\text{J}}{\text{kg}}$. Hence, when measuring the dose, the measuring volume must remain the same. Furthermore, as explained by [Ballard](#), the radiation intensity is "inversely proportional to the square of the distance" [27]. This is known as the Inverse Square Law illustrated in Figure 9. Therefore, the absorbed dose is reduced if the object moves away from the radiation source. Moreover, before reaching the tumor centroid, the radiation beams need to go through body tissues and/or organs, which makes them attenuated.

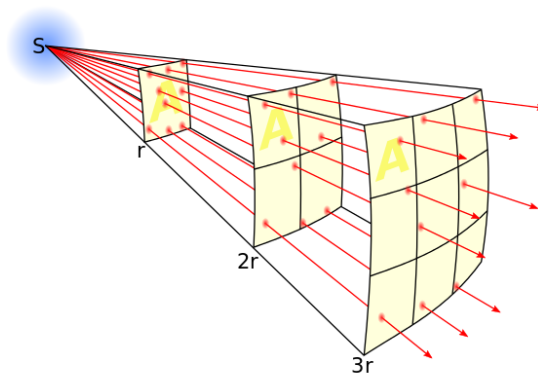


Figure 9: Inverse square law, $I \propto \frac{1}{d^2}$. [27]

As a result, per [Sibtain et al.](#), MU is needed as it indicates "how much radiation the LINAC should produce to deliver a certain amount of dose to a specific position within a patient" [18]. MU is measured by the monitor chamber which is built into the treatment head of the LINAC as:

$$MU = \frac{\text{dose per fraction (Gy)}}{\text{output dose (Gy/MU)}}, \quad (1)$$

with the following calibration conditions:

1. source to surface distance (SSD) is 100 *cm*,
2. reference depth is notated as d_{max} , whose common value is 1.3 *cm* or 5.0 *cm*,
3. open field area is $10 \times 10 \text{ cm}^2$,
4. source to reference measurement distance is $100 + d_{max} \text{ cm}$.

This can be interpreted as 1cGy is equal to 1MU at a source to measurement point distance of $100 + d_{max} \text{ cm}$ and an attenuation depth of d_{max} [18].

2.2.7 Dose distribution

The dose distribution visualizes how the body is irritated when receiving the prescribed dose. Figure 10 and Figure 11 illustrate the dose distributions of the treatment plans in Section 2.2.3 calculated by using Ethos therapy system. The Jet colormap, which is commonly referred to as "dose color wash" in radiotherapy, is used to represent the dose distributions, which means the red color area receives more doses than the blue one. As observed in Figure 10, the dose between any two beams spikes as they sum up. Hence, the distance between the beams must also be considered.

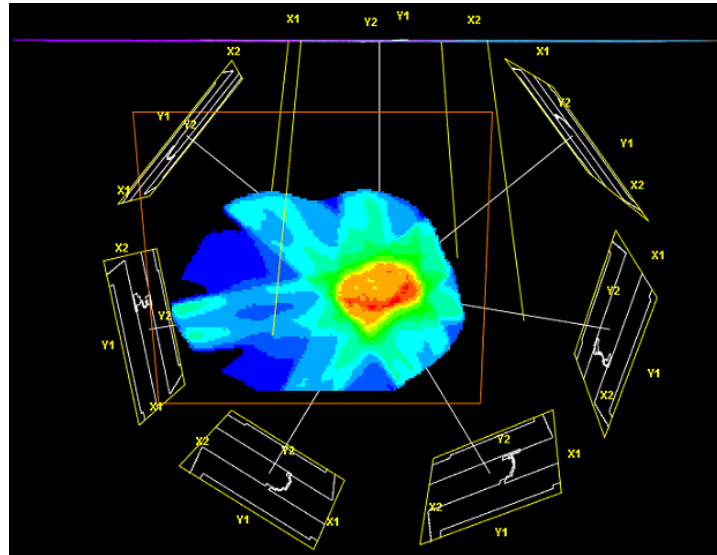


Figure 10: Dose distribution with gantry angles visualized.

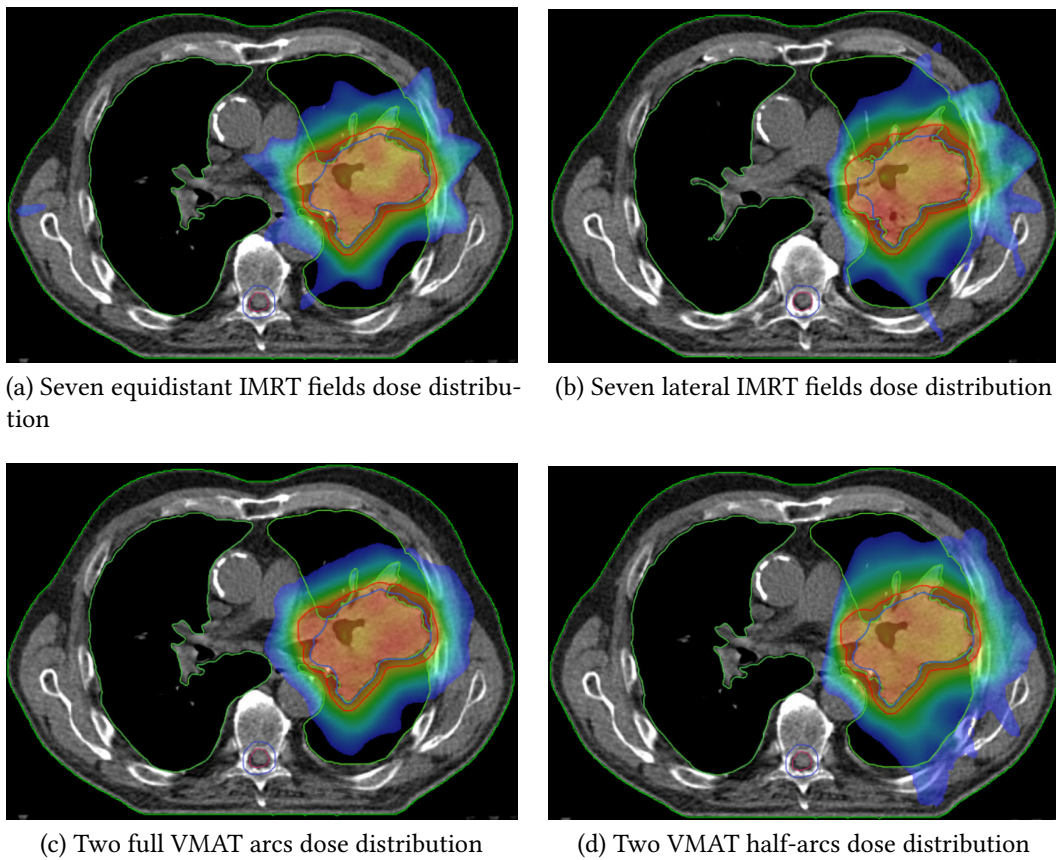


Figure 11: Dose distributions of different IMRT and VMAT plans.

It is apparent that the dose delivered by VMAT is more homogeneous than by IMRT. Besides, dose-volume histogram (DVH) as in Figure 12 is also used interchangeably.

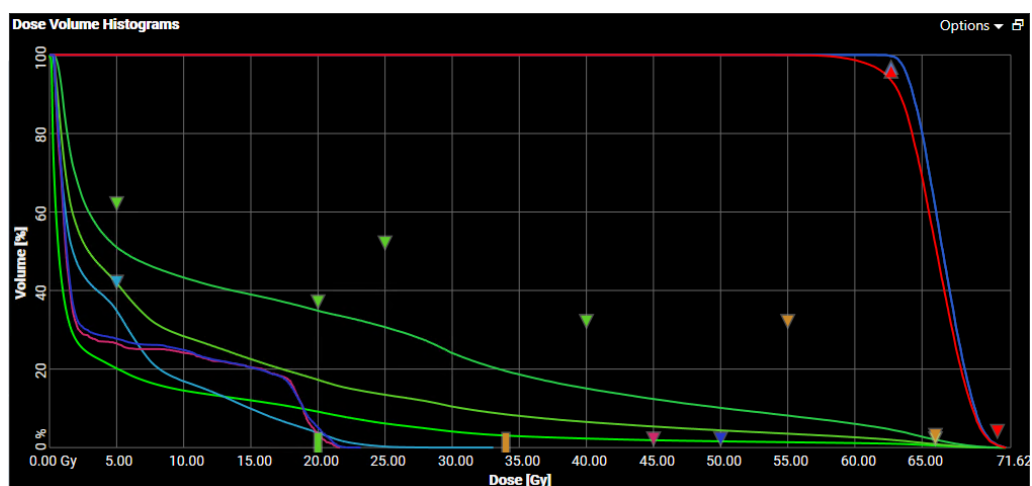


Figure 12: Seven equidistant IMRT fields DVH.

Calculating dose distribution is a part of the treatment planning step, which belongs to the radiation therapy clinical workflow.

2.2.8 Clinical workflow of radiation therapy

The clinical workflow of radiation therapy involves several complex steps and depending on the form of radiation therapy, the process will be customized for the patients. However, as described by a senior software engineer¹¹, it is expected to have five basic steps illustrated in Figure 13: initial consultation, simulation, treatment planning, treatment delivery, and post-treatment follow-up. Due to the complexity, the whole workflow requires a team of medical professionals, which includes radiation oncologists, radiation therapists, medical physicists, medical dosimetrists, and radiation oncology nurses, to plan and deliver the treatment.

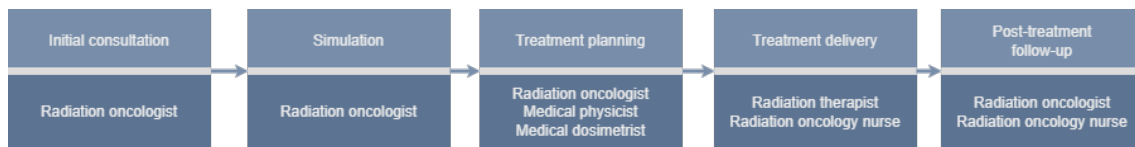


Figure 13: Simplified clinical workflow of radiation therapy.

1. **Initial consultation** is the very first step. This involves an appointment with a **radiation oncologist**, who will evaluate the patient's medical history, perform a physical exam, and review radiology images. Based on the review, if radiotherapy is determined as an appropriate treatment option, the patient will be offered an appointment for simulation.
2. **Simulation** is the second step, which allows the radiation oncologist to define the exact location of the tumor and the configuration of the treatment by using CT or MRI scans. The patient will then be placed on the treatment couch, and to maintain the patient's position during the treatment, usually, there will be customized "immobilization" devices such as mesh masks, or form-fit body molds. Additionally, the area on the body that requires treatment will be marked with a small tattoo "dot". As the treatment is delivered daily over several weeks, this will ensure that the patient is placed correctly and radiation is directed properly each day.
3. **Treatment planning** is the next step, which involves radiation oncologist, **medical physicist**, and **medical dosimetrist**. The main goal of treatment planning is to generate treatment plans that are capable of delivering a high dose of radiation to the tumor while limiting the dose received by healthy surrounding tissue. Therefore, treatment plans are personalized for each patient. Developing the treatment plan is a complex process aided by the use of computers and specialized software to outline the radiation dose, beam angles, number of fields, and other parameters specific to the patient's tumor.
4. **Treatment delivery** phase begins after treatment planning. Patients receive radiation therapy in daily sessions over several weeks. For each treatment session,

¹¹Varian Medical Systems Finland Oy

the radiation therapist is responsible for positioning the patient in the same position as in the simulation step and for delivering the radiation dose prescribed by the radiation oncologist. Normally, a session will last no more than 20 minutes and much of this time is used for accurate positioning. The prescribed dose of radiation is then delivered by a LINAC or other radiation delivery device. During the treatment delivery period, **radiation oncology nurse** will provide the patient care, support, and guidelines for skin care and nutrition.

5. **Post-treatment follow-up** is scheduled upon the completion of the treatment to assess its effectiveness and to monitor for any potential side effects. Additional diagnostics may be ordered, which include imaging scans, physical exams, and laboratory tests.

2.3 Computer graphics

“ The term computer graphics describes any use of computers to create and manipulate images. ”

Shirley et al. [28]

Even though there is no concrete definition of computer graphics, in Lehtinen's lecture [29], he mentioned: "Computer graphics means generating pictures by computation". According to Shirley et al. [28], the major areas of computer graphics consist of:

1. **Modeling** deals with the mathematical specification of shape and appearance properties in a way that can be stored on the computer. Figure 14 illustrates the 3D model of a well-known clay figurine, the "Stanford Bunny" [30], rendered by using a custom render engine compares to its photograph.
2. **Rendering** deals with the creation of shaded images from 3D computer models. This will be addressed in more detail in Section 2.3.3.
3. **Animation** is a combination of both modeling and rendering to create an illusion of motion through sequences of images.

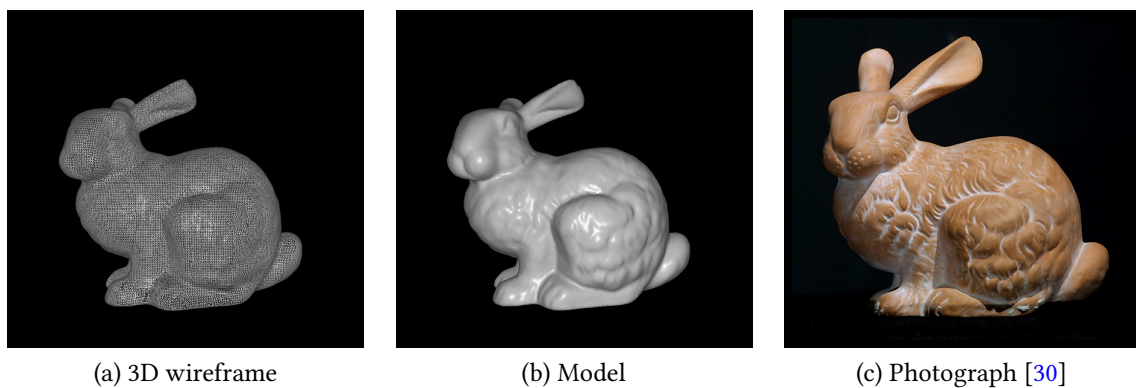


Figure 14: The "Stanford Bunny".

Visual effects, video games, information visualization, and medical imaging are some applications of computer graphics. In order to utilize and communicate with a graphics processing unit (GPU), an application programming interface (API) is needed. There are several API collections, such as Vulkan¹², Metal¹³, DirectX¹⁴, and OpenGL¹⁵. With the advancements in both hardware and software, the reality of computer graphic output has been improved significantly.

2.3.1 Viewing pipeline

Before getting into the details of the viewing pipeline, **polygon mesh** should be introduced first. Consisting of vertices, edges, and faces, a polygon mesh represents an object by mimicking its shape and surface.

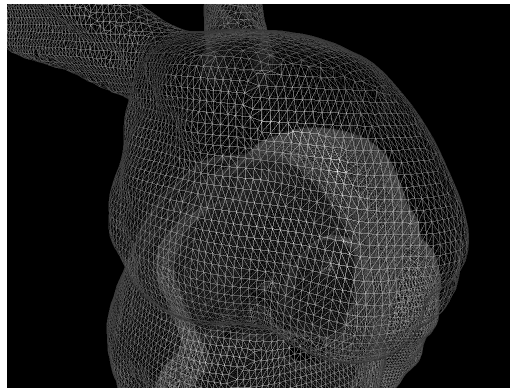


Figure 15: 3D wireframe of "Stanford Bunny".

Figure 15 is the zoom-in view of the same 3D wireframe of Stanford Bunny in Figure 14. Two things can be observed: the model itself is a collection of triangles, which is formally called **triangle mesh**, and the inside of the model is actually empty, as we are only interested in how to construct the visible surface geometry of the subject. In addition to triangle meshes, quadrilaterals, and other polygons are also used.

The viewing pipeline, which is illustrated in Figure 16, is a part of the **graphics pipeline**. There are multiple graphics pipelines depending on the API one uses. However, they are fairly similar on a high level, and they all are highly parallelized and optimized for efficient computing on GPUs.

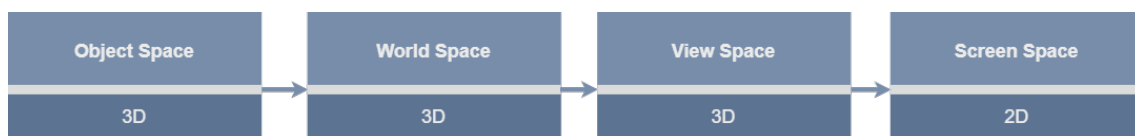


Figure 16: Viewing pipeline.

¹²<https://www.vulkan.org/>

¹³<https://developer.apple.com/metal/>

¹⁴<https://developer.nvidia.com/directx>

¹⁵<https://www.opengl.org/>

Each object has its vertices defined in its own coordinate system called **object space** to keep it isolated from other objects. The object space is usually represented in a three-dimensional Cartesian coordinate system (x, y, z) and hence, there exists an origin $(0, 0, 0)$, which is often the center of the objects. A benefit of having the object space is that the objects can be transformed individually without interfering with others [29].

A scene consists of multiple objects. Therefore, a common coordinate system to represent the relativity of the objects' positions is needed. It is called **world space** and similar to the object space, it is expressed using the three-dimensional Cartesian coordinate system, and the origin is usually located at the center of the scene. There may exist multiple object spaces, but there will be only one world space [29]. The world space is the common frame of reference for not only objects but also cameras, lights, and other elements within a scene [31].

Similar to real life, there is a need for a camera to capture the scene. The **camera space** also uses the three-dimensional Cartesian coordinate system, and the origin is the camera's position. In the camera space, objects are relatively transformed to the camera's viewpoint. This helps the rendering process to determine which objects are visible and to compute the perspective effects. By discarding the objects that are outside of the view frustum, the performance is improved and this is known as view-frustum culling [32].

Lastly, there is a **screen space** defined by the actual screen (display). Unlike others, the screen space is a two-dimensional coordinate system (x, y) with the origin $(0, 0)$ located at the top-left corner of the viewport [32] [33]. The unit of measurement in the screen space is a pixel, short for picture element. Once the objects are projected onto the screen space from the camera space, further operations can be applied, such as rasterization, texture mapping, shading, and anti-aliasing [29].

2.3.2 Transformations

In computer graphics, geometric transformations are used to change the positions, scale, and orientation of points in space. Per Lehtinen's lecture [29], these transformations are considered to be the building blocks of computer graphics, and complex ones can be built out of them:

1. **Translation** modifies the object's position while preserving its shape or orientation.
2. **Rotation** rotates the object around a specific axis or point while preserving its shape.
3. **Scaling** makes the object become larger or smaller. The shape of the object is not necessarily preserved.
4. **Reflection** produces a mirror image of an object along a specific axis and the object's shape is preserved.
5. **Shearing** slants the shape of the object along one or more axes.

6. **Planar perspective transformation** or **projective transformation** is the most general and it projects the object onto a two-dimensional plane [29]. One important characteristic of projective transformation is that the projection process simulates the behavior of human vision.

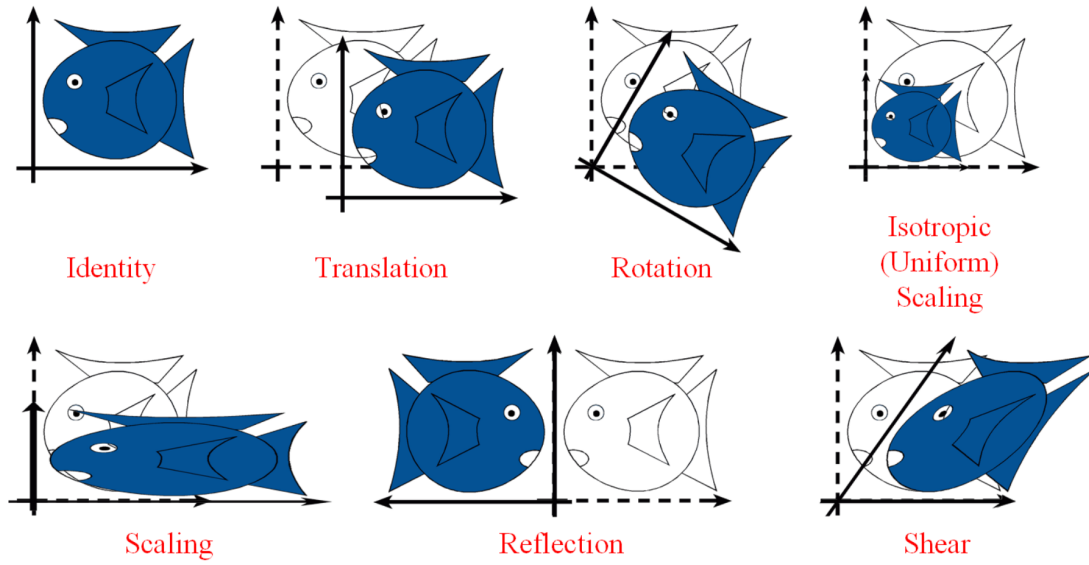


Figure 17: Examples of transformations. [29]

All transformations mentioned above can be represented using matrices. Linear transformations including rotation, scaling, reflection, and shear, can be represented as:

$$\begin{aligned}
 x' &= ax + by \\
 y' &= cx + dy \\
 \begin{bmatrix} x' \\ y' \end{bmatrix} &= \begin{bmatrix} a & b \\ c & d \end{bmatrix} \begin{bmatrix} x \\ y \end{bmatrix} \\
 p' &= Mp,
 \end{aligned} \tag{2}$$

where $p' = (x', y')$ is the new point, M is the transformation, and $p = (x, y)$ is the original point. However, affine transformations, which include all linear transformations and translation, cannot be represented in the form of $p' = Mp$ due to six degrees of freedom (DoF) - or 12 DoF in the three-dimensional space:

$$\begin{aligned}
 x' &= ax + by + e \\
 y' &= cx + dy + f \\
 \begin{bmatrix} x' \\ y' \end{bmatrix} &= \begin{bmatrix} a & b \\ c & d \end{bmatrix} \begin{bmatrix} x \\ y \end{bmatrix} + \begin{bmatrix} e \\ f \end{bmatrix} \\
 p' &= Mp + t.
 \end{aligned} \tag{3}$$

To solve the problem, **homogeneous coordinates** are used as they make the affine transformations linear in this one-higher-dimension. The homogeneous coordinates were first introduced by August Ferdinand Möbius in his *Der barycentrische Calkul* (1827; “The Calculus of Centres of Gravity”)¹⁶. Besides computer graphics, computer vision also employs homogeneous coordinates to represent projective transformations by matrices.

To convert to homogenous coordinates, an extra dimension is added:

$$\begin{bmatrix} x \\ y \end{bmatrix} \Rightarrow \begin{bmatrix} x \\ y \\ 1 \end{bmatrix}. \quad (4)$$

To convert from homogeneous coordinates:

$$\begin{bmatrix} x \\ y \\ w \end{bmatrix} \Rightarrow \begin{bmatrix} x/w \\ y/w \end{bmatrix}. \quad (5)$$

Hence, the affine transformations in Equation 3 can now be represented as:

$$\begin{bmatrix} x' \\ y' \\ 1 \end{bmatrix} = \begin{bmatrix} a & b & e \\ c & d & f \\ 0 & 0 & 1 \end{bmatrix} \begin{bmatrix} x \\ y \\ 1 \end{bmatrix} \quad (6)$$

$$p' = Mp.$$

By using homogeneous coordinates, as mentioned above, complex successive transformations can be represented easily by using matrix multiplications. It is worth noting that they are noncommutative, i.e. the order matters.

2.3.3 Rendering

“ Rendering refers to the entire process that produces color values for pixels. ”
Jaakko Lehtinen [29]

There are two major techniques for rendering, which are rasterization and ray tracing as represented in Algorithm 1 and Algorithm 2, respectively. At the first glance, the two algorithms are different. However, fundamentally, they still solve the same problems with different orders, and ultimately, this leads to the consequence that each algorithm requires different hardware to run it efficiently. Per Caulfield [34], “modern NVIDIA GPUs can generate over 100 billion rasterized pixels per second”, and the ones with specialized RTX hardware are capable of tracing “billions of rays per second”.

¹⁶<https://www.cambridge.org/core/services/aop-cambridge-core/content/view/235A89804289968FD4C285175D234A86/S0013091500030923a.pdf>

Algorithm 1 Rasterization. [29]

```

for each triangle do
  for each pixel do
    Does triangle cover pixel?
    Keep closest hit
  end for
end for

```

Algorithm 2 Ray tracing. [29]

```

for each pixel (ray) do
  for each object do
    Does ray hit object?
    Keep closest hit
  end for
end for

```

Besides, there exists the "rendering equation" that was presented by Kajiya [35] with the introduction of path tracing. The sample image in Kajiya's paper is 512 by 512 pixels and took more than 20 hours to render in 1986, which was totally impractical at that time. However, with the increase in computing power, the practical application of the technique lies on the horizon. Figure 18 illustrates the output of different rendering techniques.

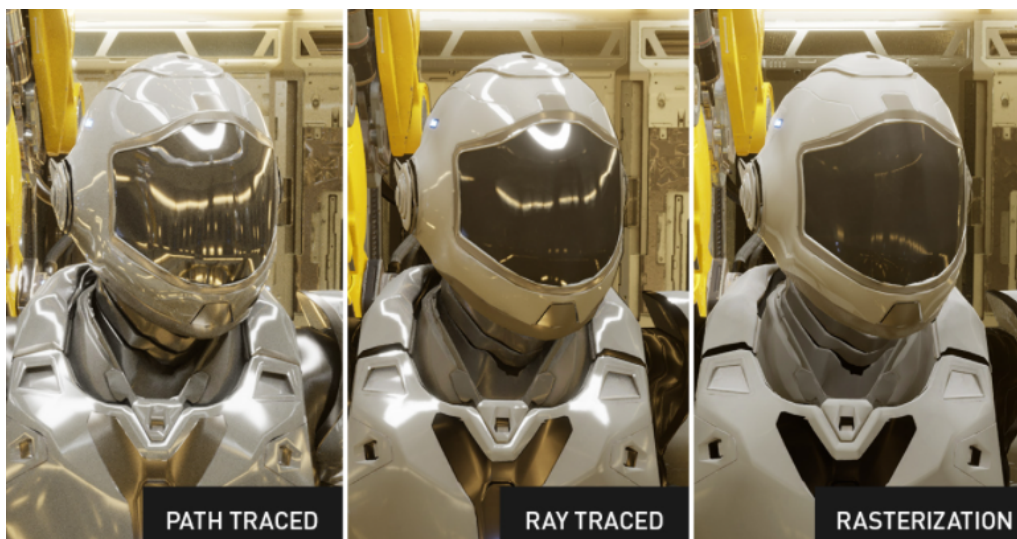


Figure 18: Renders of different rendering techniques. [34]

There are different rendering engines ranging from real-time rendering used in video games, such as Unreal Engine¹⁷ and Unity¹⁸, to offline rendering used in graphics, such

¹⁷<https://www.unrealengine.com/>

¹⁸<https://unity.com/>

as Blender¹⁹, movie production, such as V-Ray²⁰ and Arnold²¹, and animation production, such as RenderMan²² and MoonRay²³. Nevertheless, the common goal of those engines is still to determine how the scene should be visually depicted.

2.3.4 Ray tracing and ray casting

“ The ray tracing algorithm was extended and improved, giving it the power to handle many different kinds of optical effects. Today ray tracing is one of the most popular and powerful techniques in the image synthesis repertoire: it is simple, elegant, and easily implemented. ”

Andrew S. Glassner [36]

According to Hofmann [37], the principle of ray tracing was presented by Albrecht Dürer in 1525. In 1969, Arthur Appel brought ray tracing to computer graphics and applied it to computing visibility and shadows [34][38]. The very early version of ray tracing-based algorithms is non-recursive, which is called **ray casting** nowadays.

Ray casting operates in a straightforward manner. It casts one primary ray per pixel directly from the camera position to find the closest hits and does not take into account lighting effects.

Ray tracing, on the other hand, is a more advanced technique that aims to simulate the behavior of light by tracing rays and imitating their interactions with objects. Therefore, it is capable of accurately modeling complex lighting effects such as reflections, refractions, or global illumination. Figure 19 illustrates the reflection and refraction using Fresnel equations²⁴ and Phong shading²⁵.

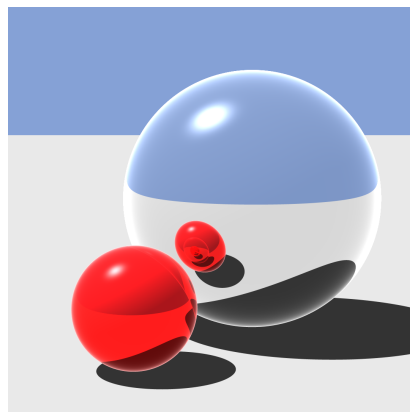


Figure 19: Illustration of reflection and refraction in ray tracing.

¹⁹<https://www.blender.org/>

²⁰<https://www.chaos.com/3d-rendering-software>

²¹<https://www.arnoldrenderer.com/>

²²<https://renderman.pixar.com/>

²³<https://openmoonray.org/>

²⁴https://graphics.stanford.edu/courses/cs148-10-summer/docs/2006--degrev--reflection_refraction.pdf

pdf

²⁵<https://stanford.edu/class/ee267/lectures/lecture3.pdf>

While both methods involve tracing rays of light, the differences in the algorithms' complexity lead to the variance in the outputs' realism. Furthermore, aliasing has been a major problem for both ray tracing and ray casting algorithms. This can be solved by stochastic sampling [36].

2.4 Machine learning

“ Machine learning is essentially a form of applied statistics with increased emphasis on the use of computers to statistically estimate complicated functions and a decreased emphasis on proving confidence intervals around these functions; ”

Goodfellow et al. [39]

Machine learning is a subset of artificial intelligence. While the concept of a machine that is capable of imitating humans starts in the early 1940s (or even sooner) [40][41], the term "machine learning" is believed to be coined by Arthur Samuel in 1959 [42]. Mitchell gave a precise definition of the "learning" part in machine learning as "A computer program is said to learn from experience E with respect to some class of tasks T and performance measure P, if its performance at tasks in T, as measured by P, improves with experience E" [43].

Machine learning is especially useful in tasks that are too complex for normal programs since it provides powerful techniques to extract valuable insights from data and to make predictions based on provided data. Hence, it has a wide range of applications across various domains, such as natural language processing, recommendation systems, and fraud detection.

2.4.1 Machine learning types

According to Bishop, machine learning algorithms "can be classified into three types: supervised learning, unsupervised learning, and reinforcement learning" [44].

1. **Supervised learning** describes algorithms that learn from labeled training data to make predictions or classifications on a new dataset. In supervised learning, the data consists of input (features) and the corresponding output (labels). Once the model is trained, new and unlabeled data can be used as input. Supervised learning can be applied to forecasting sales numbers, classifying emails as spam or non-spam, recognizing handwriting, diagnosing diseases, and many more.
2. **Unsupervised learning** is represented by algorithms that learn from unlabeled data and discover the data pattern. In unsupervised learning, the input data consists only of the features, without any associated output labels. Unsupervised learning can be used for customer segmentation, market basket analysis, text and image clustering, and recommendation systems, and is extremely useful when manually labeling the data would be impractical or infeasible.

3. **Reinforcement learning** is defined by algorithms that learn from feedback (rewards or penalties) based on their actions in an environment so that in the end, the cumulative rewards are maximized. Reinforcement learning has demonstrated its capability in game playings, such as AlphaGo²⁶, robotics, and autonomous vehicles.

There are common challenges encountered in machine learning. Addressing them often involves a combination of techniques, such as model selection, data preprocessing, and feature engineering.

1. **Imbalanced data** refers to a dataset where a class is significantly more prevalent than others. which can make the model become biased as the majority is favored. Oversampling and undersampling can be used to handle imbalanced data.
2. **Noisy data** contains errors and outliers that happens during data collection, data transmission, or even the data generating process. It can negatively impact model performance as data features might not be properly extracted. Data preprocessing and analysis techniques are necessary to deal with noisy data.
3. **Overfitting** and **underfitting** are two common phenomena occur to regression problems. They relate to the model's ability to perform on unseen data. To address overfitting and underfitting, early stopping and increase model complexity techniques can be used, respectively.

As illustrated in Figure 20, Goodfellow et al. [39] used a linear function, a quadratic function, and a polynomial of degree 9, respectively, to fit the data that was generated by a quadratic function.

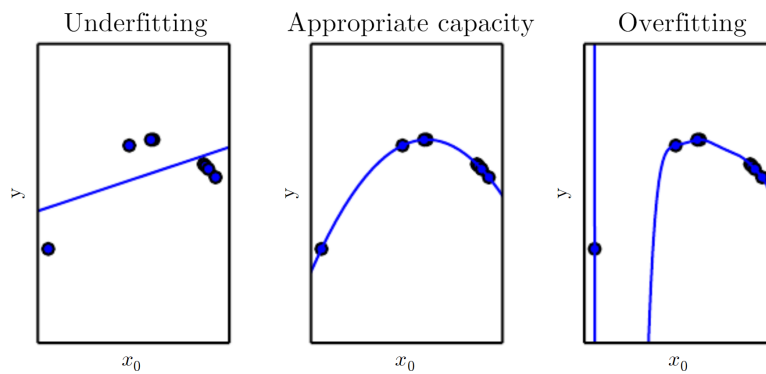


Figure 20: Illustration of algorithm's capacity. [39]

Besides the mentioned techniques, appropriate evaluation methods have a huge impact on model performance. **Root mean square error** (RMSE) is a commonly used metric in linear regression problems. It penalizes large errors more heavily than small errors due to the squaring of the differences. It is defined as:

²⁶<https://www.deepmind.com/research/highlighted-research/alphago>

$$RMSE = \sqrt{\frac{1}{N} \sum_{i=1}^N (y_i - \hat{y}_i)^2}, \quad (7)$$

where N is the total number of the data points, y_i is the observed label of i -th data point, \hat{y}_i is the predicted label of i -th data point. The lower RMSE, the better the model performance is. Figure 21 illustrates how RMSE works. The blue line is the regression line, green dots are data points and purple lines represent the distances, i.e. differences between the real labels and the predicted labels.

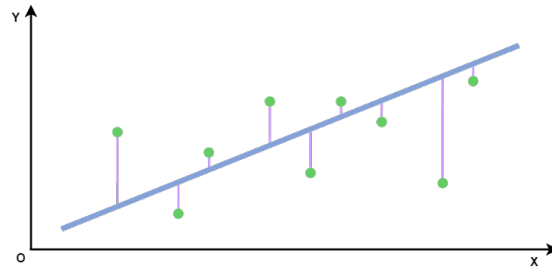


Figure 21: Illustration of how RMSE works.

For binary classification, **confusion matrix** is a useful tool for understanding the accuracy, precision, recall, and other performance metrics of a classifier. For example, precision or positive predictive value can be calculated as:

$$precision = \frac{N_{TP}}{N_{TP} + N_{FP}}, \quad (8)$$

where N_{TP} is the total number of true positive predictions, and N_{FP} is the total number of false positive predictions.

		Actual class	
		Yes	No
Predicted class	Yes	True positive (TP)	False positive (FP)
	No	False negative (FN)	True negative (TN)

Figure 22: Confusion matrix. [45]

2.4.2 Clustering

“ The goal in such unsupervised learning problems may be to discover groups of similar examples within the data, where it is called clustering, ... ”

Bishop [44]

The main goal of clustering is to divide a dataset into groups, where the data points within each group should be as similar as possible and the data points from different groups should be as dissimilar as possible. There are two major types of clustering:

1. **Hard clustering** where each data point belongs to exactly one cluster.
2. **Soft clustering** where each data point can belong to multiple clusters with different probabilities.

There are several clustering algorithms and their variations; and depending on the data types and the task requirements, a suitable one should be selected. Some common types of clustering are centroid-based clustering, density-based clustering, and hierarchical clustering.

K-means is a centroid-based clustering algorithm [46]. Its goal is to partition the data into k distinct clusters, where k is a predefined number. The algorithm works iteratively by initially randomly assigning k cluster centroids and then updating them until convergence. Each data point is assigned to the cluster with the closest centroid based on predefined distance metrics. K-means seeks to minimize the sum of squared error (SSE) between data points and the cluster centroids. SSE is calculated as:

$$SSE = \sum_{i=1}^K (x_i - \hat{x})^2, \quad (9)$$

where K is the number of data points, x_i is an data point and \hat{x} is the cluster centroid nearest to x_i . The advantages of the K-means algorithm are it is guaranteed for the algorithm to converge and it can scale to large datasets [47]. However, its disadvantages are the number of clusters "k" needs to be selected manually, it is dependent on the initial values and outliers can impact the clusters significantly [47].

2.4.3 Clustering distance metrics

The similarity or dissimilarity between data points is measured by using distance metrics. There are several distance metrics and different metrics are suitable for different data types.

Cosine similarity measures the similarity between two non-zero vectors as:

$$\text{cosine_similarity} = \cos(\theta) = \frac{a \cdot b}{\|a\| \|b\|}, \quad (10)$$

where a and b are n -dimensional vectors. Hence, the cosine similarity always belongs to the interval $[-1, 1]$, where two like vectors have a cosine similarity of 1, and two opposite vectors have a similarity of -1 .

Haversine distance or **great circle distance** calculates the angular distance between two points on a sphere surface given the longitudes and latitudes as [48]:

$$d(a, b) = 2 \arcsin \left[\sqrt{\sin^2((x_1 - y_1)/2) + \cos(x_1) \cos(y_1) \sin^2((x_2 - y_2)/2)} \right], \quad (11)$$

where (x_1, y_1) is the latitude and longitude in radians of point a and (x_2, y_2) is the latitude and longitude in radians of point b .

Euclidean distance measures the straight line distance between two points as:

$$d(a, b) = \sqrt{(b_1 - a_1)^2 + (b_2 - a_2)^2 + \cdots + (b_n - a_n)^2}, \quad (12)$$

where (a_1, a_2, \dots, a_n) is the Cartesian coordinates of point a and (b_1, b_2, \dots, b_n) is the Cartesian coordinates of point b in an n -dimensional Euclidean space.

Manhattan distance or **cityblock distance** or **L1 distance** calculates the sum of the absolute differences between the coordinates of two points as:

$$d(a, b) = |b_1 - a_1| + |b_2 - a_2| + \cdots + |b_n - a_n|, \quad (13)$$

where (a_1, a_2, \dots, a_n) is the Cartesian coordinates of point a and (b_1, b_2, \dots, b_n) is the Cartesian coordinates of point b in an n -dimensional Euclidean space.

Figure 23 illustrates the Euclidean distance, whose color is purple, and Manhattan distance, whose color is green, between points A and B.

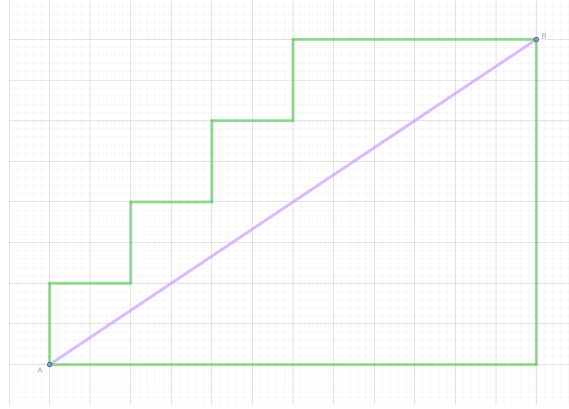


Figure 23: Euclidean distance and Manhattan distance.

2.4.4 Clustering evaluation metrics

In machine learning, it is important to select a proper measurement for quantitatively evaluating the correctness of the model output. These metrics provide objective measures which support the comparison between different models or variations of the same model. For clustering problems without ground-truth labels, the metrics that are listed below can be used for quantitative comparisons.

Silhouette index was introduced by Rousseeuw in 1987 [49]. It measures the compactness and separation of clusters in a dataset. The Silhouette index of a point x is calculated as [50]:

$$S(x) = \begin{cases} 0 & \text{if } x \text{ is a cluster of its own} \\ \frac{b-a}{\max\{a,b\}} & \text{otherwise} \end{cases}, \quad (14)$$

where a is the average distance between the data point and all other data points in the same cluster, $a = \text{avg}\{d(x, y) | x \in C, y \in C\}$, and b is the average distance between the data point and all data points in the nearest neighboring cluster, $b = \min_q \text{avg}\{d(x, y) | x \in$

$C, y \in C_q, C \neq C_q\}$. $S(x)$ ranges from -1 to 1 , where 1 indicates that the data point is well clustered and lies far away from the neighboring clusters, and -1 indicates that the data point is likely assigned to a wrong cluster.

Davies–Bouldin index was jointly introduced by Davies and Bouldin in 1979 [51]. It also measures the compactness and separation of clusters similar to the Silhouette index. Davies-Bouldin index is calculated as [50]:

$$S_{DB} = \frac{1}{K} \sum_{i=1}^K \max_{j \neq i} \frac{S_i + S_j}{D_{ij}}, \quad (15)$$

where $S_i = \left(\frac{1}{|C_i|} \sum_{x \in C_i} d^t(x, C_i) \right)^{\frac{1}{t}}$ stands for within-cluster scatter with distance d^t and typical value for t -norm is 2, K is the size of the cluster, $D_{ij} = L_p(C_i, C_j)$ represents the separation between clusters C_i and C_j . S_{DB} ranges from 0 to infinity where the smaller the value, the better the data points were clustered.

3 Research materials

“ If we have data, let’s look at data.
If all we have are opinions, let’s go with mine.”

Jim Barksdale

This chapter describes the data that is used to evaluate the reverse beam method, and the data that is generated out of the original dataset to further improve the proposed method. Additionally, the data processing step is elaborated in detail and the environment setup is briefly mentioned.

3.1 NSCLC-Radiomics dataset

Due to the nature of this work, the dataset must have DICOM Radiotherapy Structure Sets (RTSTRUCTs) to construct the 3D models of the tumors and OARs. The NSCLC-Radiomics²⁷ dataset from TCIA is suitable as it has not only CT scans but also the necessary structure sets. Additionally, NSCLC stands for non-small cell lung cancer, which is the most common type of lung cancer as 85-90% of lung cancers are NSCLC [52]. Besides, small cell lung cancer (SCLC) is less common and the term “small cell” refers to the size and shape of the cells when viewed under a microscope [52].

3.1.1 Data description

The NSCLC-Radiomics dataset is a collection of pretreatment CT scans and structure sets from 422 non-small cell lung cancer patients. Patients are labeled as "LUNG1-xyz", where "xyz" is a unique increasing index. It should be noted that the data is anonymized, which means the patient’s identity is completely removed and cannot be traced back. Because of time constraints and resource limitations, only the first 50 patients (except patient LUNG1-035, whose CT scans cannot be connected to ARIA²⁸ oncology information system, and patient LUNG1-050, whose contour data was missing, were replaced by patients LUNG1-051 and LUNG1-052) were used.

The CT scans were acquired by using several different scanners: Siemens Biograph 40, Siemens Sensation Open, Siemens Sensation 16, and CMS XiO. All images have 512 pixels for the width and 512 pixels for the height. The number of CT scans of each patient varies from 82 to 197 slices.

The 3D volume of the primary gross tumor volume, which is labeled as "GTV-1", and the selected anatomical structures (the heart, lungs, spinal cord, and esophagus in this study) were manually delineated by a radiation oncologist. The number of CT scans varies from patient to patient, and not all patients have all listed organs contoured. For example, patient LUNG1-001 has 134 CT slices and has contours for the lungs and spinal cord. For visibility, only 10 slices out of 21 slices that contain the tumor from patient LUNG1-001 are shown in Figure 24.

²⁷<https://doi.org/10.7937/K9/TCIA.2015.PF0M9REI>

²⁸Varian Medical Systems, Palo Alto, CA

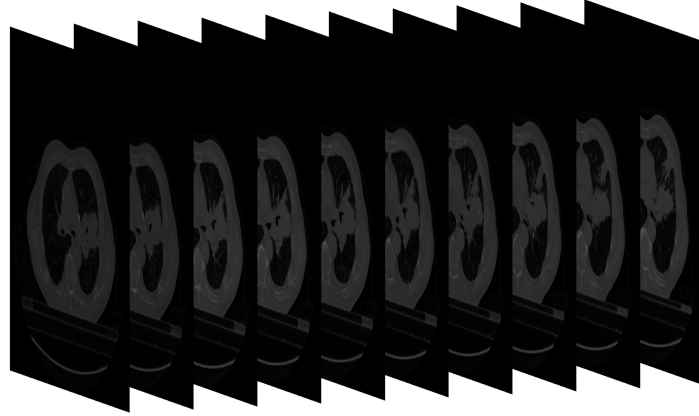


Figure 24: Example of CT scans of patient LUNG1-001 of NSCLC-Radiomics dataset.

3.1.2 Data processing

Even though DICOM is an international standard, different medical centers have different conventions for naming and organizing DICOM files. It is common that structure sets are stored in different DICOM files than the ones that store CT scans, which is again not distinguishable based solely on the file's name. Hence, in order to query the structure sets, the whole DICOM directory and its subfolders must be read and processed, which causes a big overhead for the whole process. However, this step needs to be performed only once. Afterward, the information on the region of interest (ROI), which means the tumors and OARs, is available in **ROI Contour Module**²⁹ from the RTSTRUCT files:

1. Coordinates of the contours defined by sequences of (x, y, z) triplets in the Patient-Based Coordinate System³⁰ are extracted from **Contour Data**³¹.
2. Color representations of the contours defined by RGB triplet ranging from 0 to 255 are extracted from **ROI Display Color**³².

Figure 25 represents the contour data that was found in the RTSTRUCT file of patient LUNG1-001. The spinal cord, the left lung, and the right lung were contoured for all patients. Additionally, the heart and esophagus were contoured for 30 and 41 patients, respectively. 23 patients have more than one tumor contoured. However, due to the scope of this thesis, only the "GTV-1" volumes were processed.

²⁹https://dicom.nema.org/medical/dicom/current/output/chtml/part03/sect_C.8.8.6.html

³⁰https://dicom.nema.org/medical/dicom/current/output/chtml/part03/sect_C.7.6.2.html

³¹Tag (3006,0050)

³²Tag (3006,002A)

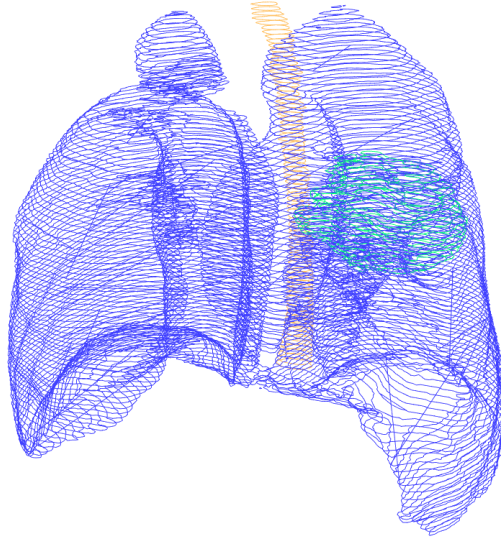


Figure 25: Patient LUNG1-001 ROIs.

In order to draw the contours on top of the CT scans for better visualization, the contour data, which is stored in Patient-Based Coordinate System, needs to be converted by using the following conversion:

$$(x, y)_{ICS} = \frac{(x, y)_{PBCS} - (O_x, O_y)_{PBCS}}{ratio}, \quad (16)$$

where $(x, y)_{ICS}$ is the contour data in the Image Coordinate System, $(x, y)_{PBCS}$ is the Contour Data (contour data in the Patient-Based Coordinate System), O_{PBCS} is the Image Position (Patient), and *ratio* is the Pixel Spacing. Different CT scans of the same patient will have their own O_{PBCS} . However, the (x, y) values should be the same while the z -value changes. It is worth emphasizing again that the images of the CT scans and the contour have different origins, the upper left-hand corner, and the lower left-hand corner, respectively.

Hence, more information can be utilized, and this time it comes from **Image Plane Module**³³ in the CT scans:

1. The upper left-hand corner coordinates of the CT images in the Patient-Based Coordinate System are retrieved from **Image Position (Patient)**³⁴.
2. Physical distance in mm between the center of each pixel, specified by a numeric pair (width and height) is retrieved from **Pixel Spacing**³⁵.
3. The order of the CT scans is determined by **Slice Location**³⁶, which matches the z -value of the contour data without performing any conversions.

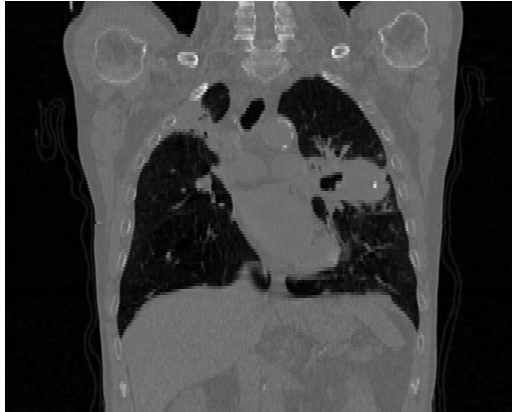
³³https://dicom.nema.org/medical/dicom/current/output/chtml/part03/sect_C.7.6.2.html

³⁴Tag (0020,0032)

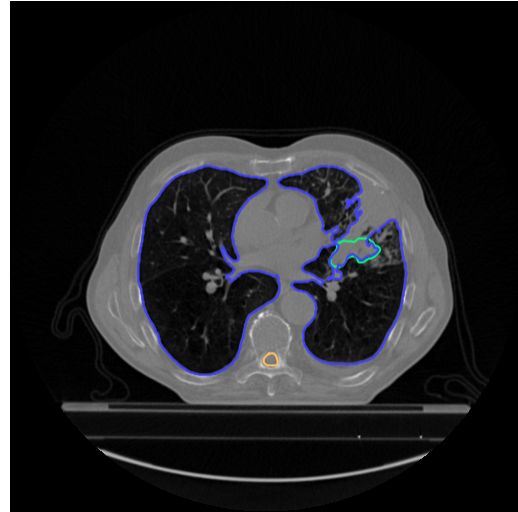
³⁵Tag (0028,0030)

³⁶Tag (0020,1041)

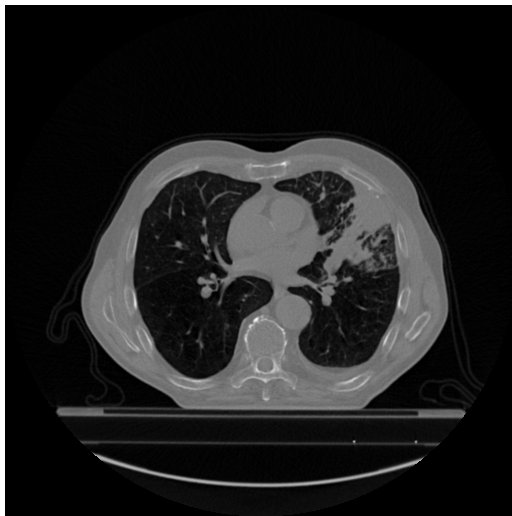
After performing all necessary conversions, Figure 26 illustrates the CT slices of patient LUNG1-001 in different view planes, with the ROI contours shown in the transversal view.



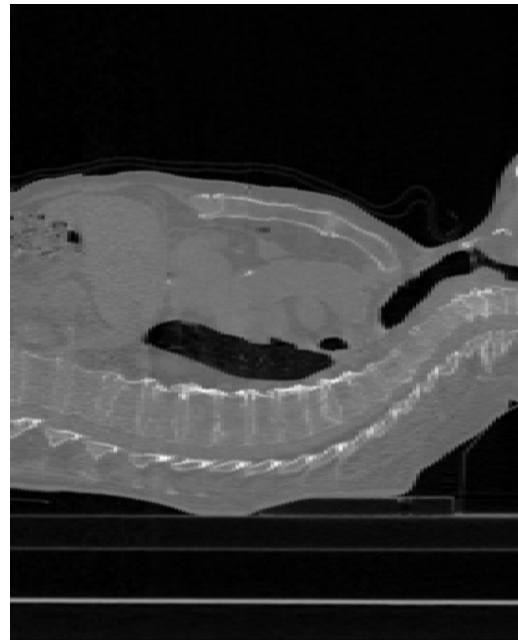
(a) Frontal view



(b) A CT slice with tumor and OARs contoured



(c) Transversal view



(d) Sagittal view

Figure 26: Images of CT slices of patient LUNG1-001.

These CT scans use **MONOCHROME2** standard defined in **Photometric Interpretation**³⁷. Hence, it can be interpreted in a way that bones, calcifications, and metal objects have a brighter color while soft tissue has a darker one [53].

³⁷Tag (0028,0004)

3.2 Radiotherapy plans and doses dataset

In order to analyze the relation between good gantry angles and the plan's properties, radiotherapy plans (RTPLANS) and the corresponding radiotherapy dose (RTDOSEs) are needed. From this point onward, this dataset will be referenced as the RTPD dataset.

The RTPD dataset is a collection of 19.500 IMRT RTPLANS and RTDOSEs that were generated using Ethos therapy system for 50 patients mentioned in Section 3.1. It should be stated clearly that they are not state-of-the-art plans and were not used clinically. However, they were still optimized with the clinical OAR constraints shown in Table 1 and if the contour of an OAR is missing, its goal will be omitted. These clinical goals were provided by a medical physicist³⁸ and were used specifically for this NSCLC-Radiomics dataset. The prescribed dose is 66 *Gy* delivered in 33 fractions using 6 *MV* photons for all plans. The PTV is derived from the GTV with 0.5 *cm* of margin.

Structure	Goal			Priority
PTV	D98.0 %	>	95.0 %	1-Most important
	D2.0 %	<	107.0 %	2-Very important
Spinal canal	D0.1 %	<	45.0 <i>Gy</i>	1-Most important
Esophagus	D1.0 %	<	66.0 <i>Gy</i>	2-Very important
	V55.0 <i>Gy</i>	<	30.0 %	3-Important
	Dmean	<	34.0 <i>Gy</i>	3-Important
Heart	V25.0 <i>Gy</i>	<	50.0 %	2-Very important
	V40.0 <i>Gy</i>	<	30.0 %	3-Important
Both lungs	Dmean	<	20.0 <i>Gy</i>	3-Important
	V20.0 <i>Gy</i>	<	35.0 %	3-Important
	V5.0 <i>Gy</i>	<	60.0 %	3-Important
Lung (left) ¹	V5.0 <i>Gy</i>	<	40.0 %	2-Very important
Lung (right) ²	V5.0 <i>Gy</i>	<	40.0 %	2-Very important

1 Left and bilateral lung cancers will not have the "Lung (left)" goal.

2 Right and bilateral lung cancers will not have the "Lung (right)" goal.

Table 1: Clinical goals for the generated treatment plans.

The clinical goals are interpreted as: the dose received by 98 % of the PTV must be more than 95 % of the prescribed dose (D98.0 % > 95.0 %); the dose received by 2 % of the PTV must not exceed 107 % of the prescribed dose (D2.0 % < 107.0 %); the dose received by 0.1 % of the spinal canal must be less than 45.0 *Gy* (D0.1 % < 45.0 *Gy*); the dose received by 1.0 % of the esophagus must be less than 66.0 *Gy* (D1.0 % < 66.0 *Gy*); the volume of the esophagus receiving 55.0 *Gy* must be less than 30.0 % (V55.0 *Gy* < 30.0 %); the mean dose receiving by the esophagus must be less than 34.0 *Gy* (Dmean < 34.0 *Gy*); the volume of the heart receiving 25.0 *Gy* must be less than 50.0 % (V25.0 *Gy* < 50.0 %); the volume of the heart receiving 40.0 *Gy* must be less than 30.0 % (V40.0 *Gy* < 30.0 %); the mean dose received by both lungs must be less than 20.0 *Gy* (Dmean < 20.0 *Gy*); the volume of both lungs receiving 20.0 *Gy* must be less than 35.0 % (V20.0 *Gy* < 35.0 %);

³⁸Varian Medical Systems Finland Oy

the volume of both lungs receiving 5.0 Gy must be less than 60.0 % ($V_{5.0 Gy} < 60.0\%$); the volume of the left lung receiving 5.0 Gy must be less than 40.0 % ($V_{5.0 Gy} < 40.0\%$); the volume of the right lung receiving 5.0 Gy must be less than 40 % ($V_{5.0 Gy} < 40.0\%$).

The RTPD dataset is a collection of individual patient's IMRT treatment plans with the following **Gantry Angle**³⁹ setup:

1. Plans that have only one beam and all 360 angles were calculated separately.
2. 30 plans that have 12 equidistant fields, where all gantry angles are increased by $i \in [0, 29]$ simultaneously and synchronously.

As mentioned in Section 2.2.4, the collimator setup also impacts the treatment plan quality. Figure 27 illustrates MLC sequences where the MLC, whose colors are purple, pink, blue, and grey, fits the shape of the tumor, whose color is red. Since it is not in the scope of the thesis, and to make the setup of all plans as similar as possible, the collimator angle⁴⁰ of 45° was used. Li et al. [54] states that the angle yields an optimal result for prostate VMAT treatment plans and, as the comparison in Figure 27 shows, it is also a good setup for the IMRT plans in this work. However, unlike the collimator angle, the collimator movements⁴¹ need to be strictly optimized based on the tumor shape, which was done by using the Ethos therapy system algorithm.

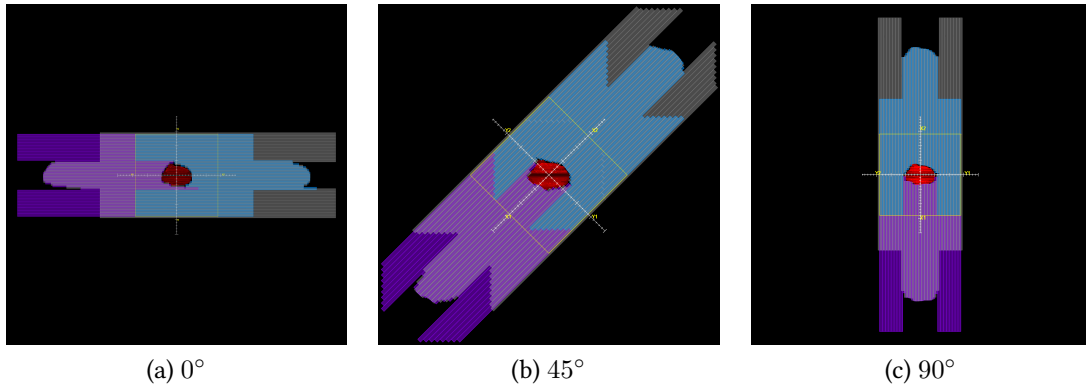


Figure 27: Different collimator angles targeting LUNG1-001 PTV.

3.3 Data analysis

The analyzing step was done to find any abnormalities in the datasets. There is a gender imbalance, which is explainable, in the selected NSCLC-Radiomics dataset: 10 females and 40 males. According to McDowell [55]: "Historically, lung cancer rates have been higher in men mainly because of their smoking patterns". For the female patients, there are five cases of left lung cancer, four cases of right lung cancer, and one case of bilateral cancer. For the male patients, there are 10, 27, and 3 cases, respectively. There are studies

³⁹Tag (300A, 011E)

⁴⁰Beam Limiting Device Angle - Tag (300A, 0120)

⁴¹Control Point Sequence - Tag (300A, 0111)

showing that gender plays a critical role in thoracic malignancies and immunotherapy [56], [57]. However, as the same research for radiotherapy is limited, gender will not be taken into account in this thesis.

The left and right lungs differ in size and shape to accommodate other organs situated in the thoracic cavity. The right lung is divided into three lobes and is shorter than the left lung due to the liver underneath it. The left lung consists of two lobes and is slightly smaller than the right lung allowing room for the heart [52]. Figure 28 represents the tumor centroid coordinates in $x - y$ and $z - y$ axes. It is clear that the tumor centroids are clustered according to the lung side as expected. Even though the tumor centroids have a variety of z -values, the distribution density of the left lung tumors is higher than the right ones on the $x - y$ axis. Figure 29 shows that there is no tumor that is too close to any OARs indicating that good beam angles can be found for most (if not all) patients.

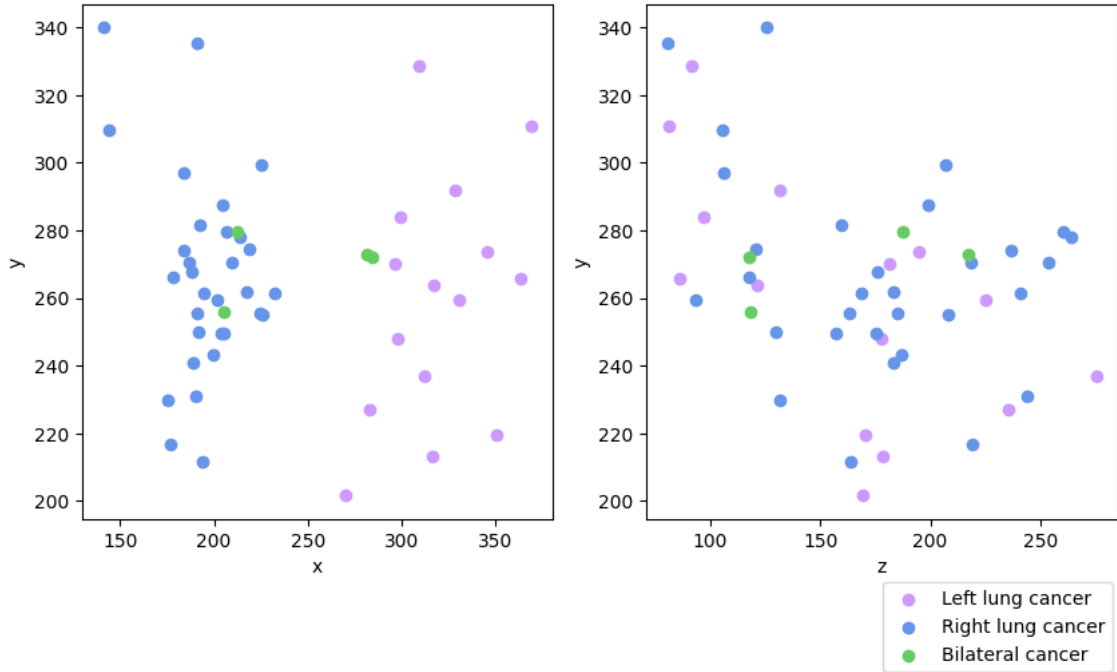


Figure 28: Tumor centroids in the Patient-Based Coordinate System represented in 2D.

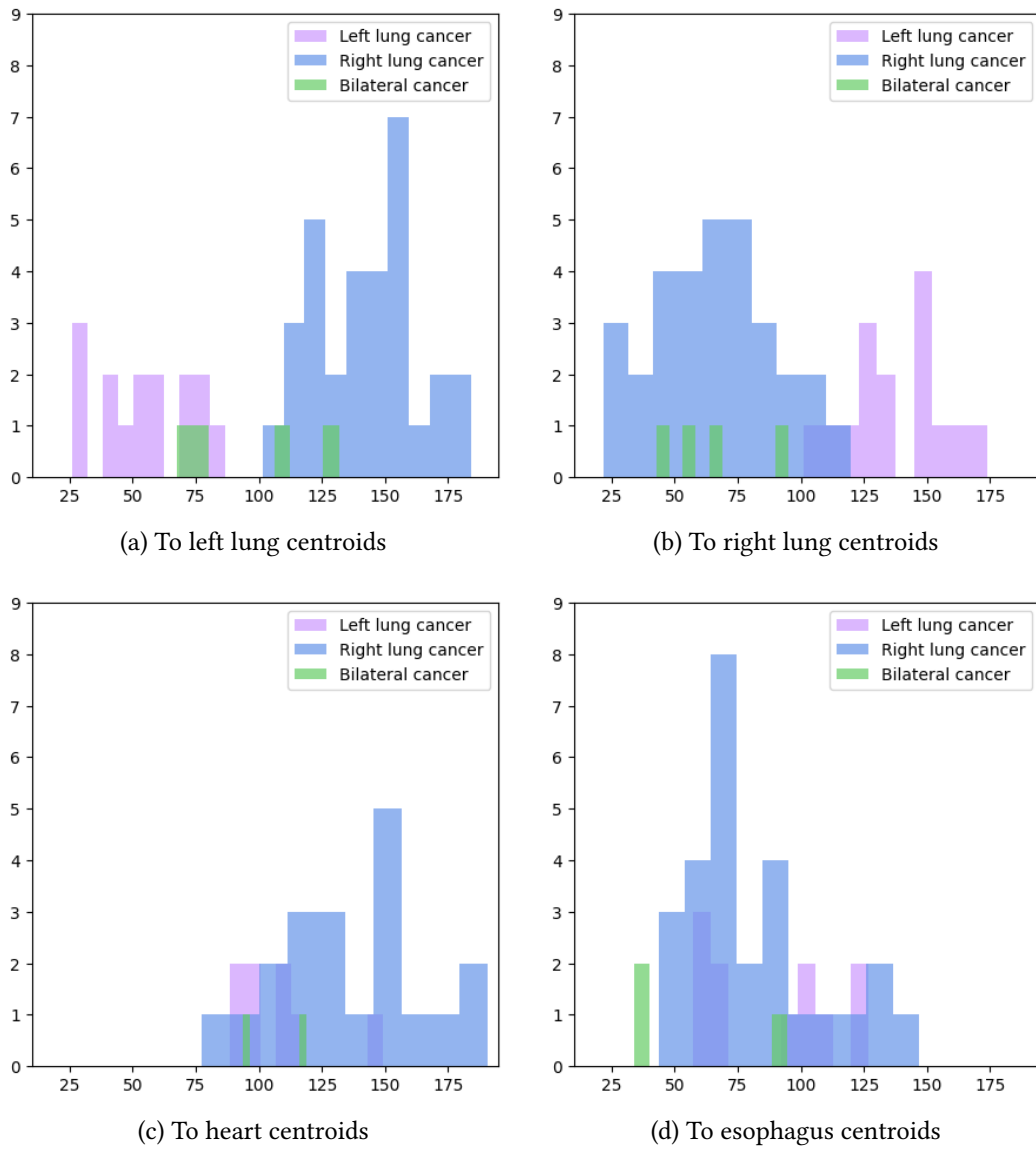


Figure 29: Histogram of the distance in mm between tumor centroids and OARs centroids.

The average magnitude of MU for IMRT plans with one field and 12 equidistant fields is illustrated by Figure 30. The Jet colormap is used to represent the MU magnitude, which means the gantry angles that have the red color has higher MU than the blue ones. The statistic of MU is presented in Table 2.

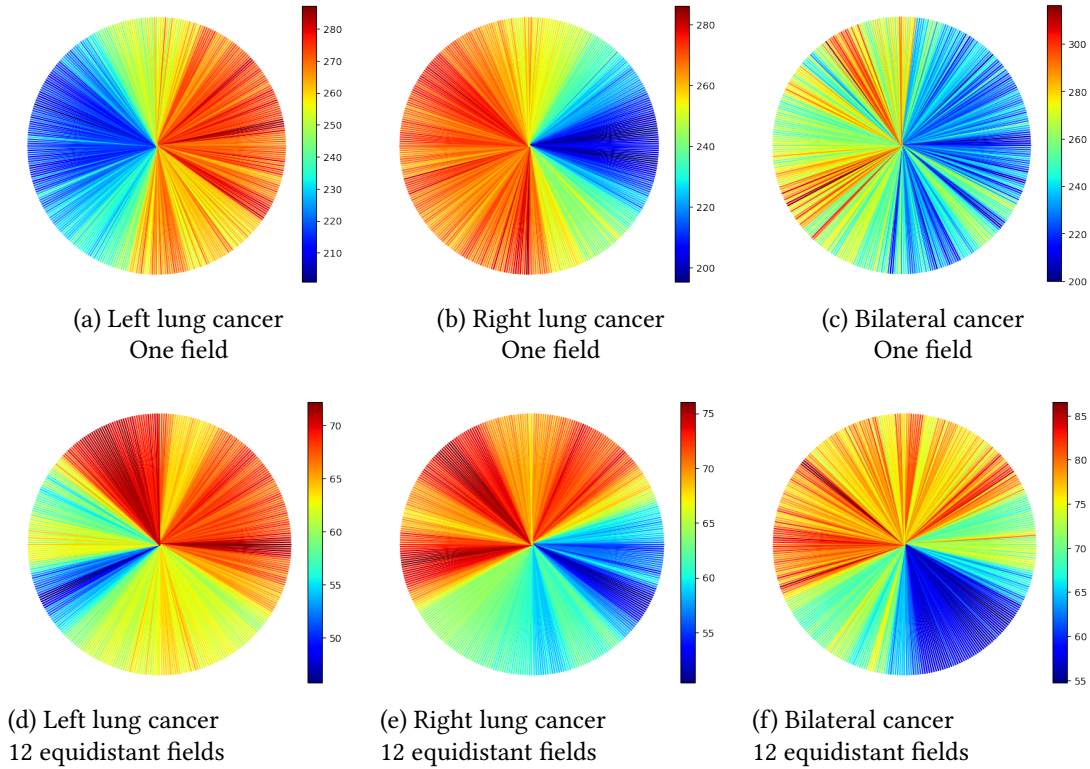


Figure 30: Heatmap of the average magnitude of MU for IMRT plans with one field and with 12 equidistant fields.

Plan type	Cancer site	Min	Max	Mean
IMRT plan with one field	Left lung cancer	128.6	440.5	249.4
	Right lung cancer	142.8	613.9	250.2
	Bilateral cancer	140.3	503.9	252.3
IMRT plan with 12 equidistant fields	Left lung cancer	0.6	118.5	63.6
	Right lung cancer	12.6	172.1	65.8
	Bilateral cancer	20.2	167.7	72.1

Table 2: MU statistics.

3.4 Development setup

Both cloud computing and local workstation were used in this work. Their configurations were as follows:

1. The VMWare vCloud environment consists of Intel Xeon 86 CPUs @ 3.0Ghz and 400GB of RAM. It has ARIA oncology information system and Ethos therapy system installed and configured. As the Ethos therapy system algorithm requires the data to be in its convention, the NSCLC-Radiomics dataset cannot be used

directly to generate new treatment plans. A new patient record must be created first and associated with the corresponding CT scans and RTSTRUCT file in ARIA oncology information system. Then, from Ethos therapy system, the newly created record will be fetched and a new treatment plan can be assigned to the patient. As mentioned in Section 2.2.5 and further elaborated in Section 3.2, the region receiving the prescribed dose is PTV, not GTV, Ethos therapy system will automatically derive the required PTV from the given "GTV-1". After this, the "usable" patient model will be exported to be used in the local environment.

2. The local workstation contains Intel Xeon 12 CPUs @ 3.2GHz with 64GB of RAM and Nvidia RTX A3000. As generating treatment plans and calculating dose distributions are significantly faster with a GPU than with a CPU, the local environment was utilized for these tasks with the exported patient model mentioned above. Additionally, this machine was also used to evaluate the algorithms.

4 Methods

In this chapter, a brief explanation of the existing techniques which are used to generate beam geometries is provided. Based on this, a new method that aims to improve performance and plan quality by using ray casting and machine learning is described in detail and accompanied by the pseudo-code.

4.1 Existing methods

As mentioned by Webb [58], there were several approaches to improve the quality of treatment plans by optimizing beam direction. A technique introduced by Pugachev and Xing was implemented inside the PLUNC⁴² planning system [58]. It employs the pseudo beam's eye-view optimization, which was developed also by Pugachev and Xing, with prior knowledge (Bayesian priors) of geometry and dosimetry for an accurate estimation. However, the technique was resource-demanding and took more than two hours on a fast workstation. The authors concluded that "the problems of optimizing beam profiles and beam directions in IMRT are coupled" and "individualized beam configurations were needed to maximally utilize the technical capacity of IMRT" [58].

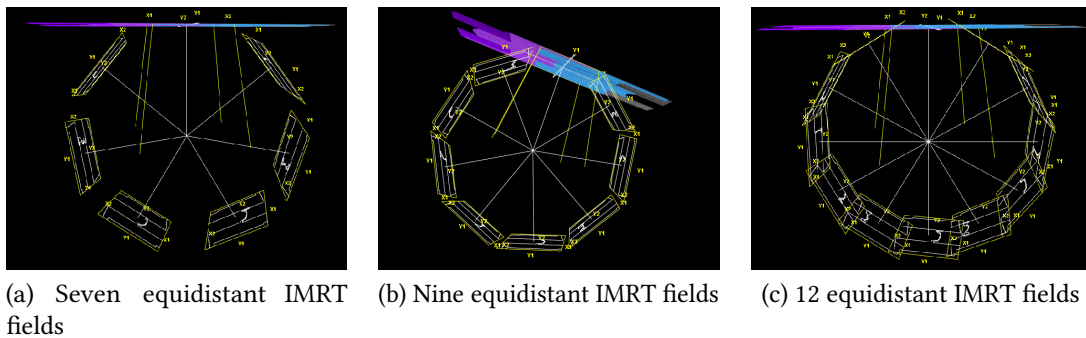


Figure 31: Beam geometry of different IMRT plans, which are aligned with the gantry angle 0° placed at straight vertical.

On Ethos therapy system, the IMRT plans with equidistant fields are focused and the beam angles are fixed. It means that the beams will be distanced equally by 50° , 40° , and 30° for 7, 9, and 12 equidistant IMRT fields plans, respectively. They are illustrated in Figure 31. By doing this, the plan generation process is sped up, but it is arguable whether the plan quality is maintained.

4.2 Reverse beam

To select gantry angles for an IMRT plan, a straightforward method is to construct the three-dimensional models of GTV and OARs from imaging scans and then perform calculations in three-dimensional space. Even though this idea might yield a high-quality

⁴²PLUNC had been developed by the University of North Carolina since 1985 for research and educational purposes, and was retired from service in 2015.

plan, it is computationally demanding as there is a large number of combinations to go through.

Hence, a new solution, which is called **reverse beam**, is proposed and studied in this thesis. The method consists of two stages: angle discovery and angle selection. The simplified acceptance criteria listed below should be followed:

1. all OARs must not receive any radiation doses,
2. doses in other areas should be minimized as much as possible,
3. 100% of tumor surface area is covered by radiation beams,

to mitigate side effects and even prevent health complications from the treatment as mentioned in Section 2.2.5. They are prioritized in the given order and will be mentioned across the method.

4.2.1 Angle discovery

It is a natural approach to simulate radiation beams from the gantry targeting the tumor. Instead of starting from the outside, the process could also start from the inside out, meaning that the beams are now emitted from the tumor itself. By doing this, all beams are guaranteed to reach the target from a good angle. This step is inspired by the ray casting technique which was described in Section 2.3. Additionally, performance can be improved as the computations are still performed in the three-dimensional coordinate system. Hence, an algorithm for **dimension reduction** is employed. The z -value is selected for the truncation because it tends to be the same for all beams since normally the tumor has only one centroid. The data loss caused by the z -value truncation will be discussed in Chapter 6.

To loosely encode the z -value for dimension reduction, Algorithm 3 is used to calculate the **opacity** of a pixel. The denser the tissue along the z -axis, the higher the opacity value is. The higher the opacity of a point, the lesser light will pass through. This follows the MONOCHROME2 standard specified in Section 3.1.2. The value is guaranteed to be in the range $[0, 1]$. The algorithm consists of two nearly identical loops to avoid the tumor opacity from being overridden. Additionally, the opacity of the OAR containing the tumor needs to be lower than other OARs and higher than the tumor values. The reason is that while we want to avoid damaging the OAR as much as possible, the beams cannot reach the tumor without irradiating the mentioned organ.

The result of Algorithm 3 is illustrated in Figure 32. All CT slices that contain the tumor have been blended together with the opacity map to create the final fusion image. The advantage of the fusion image is that both the tumor and OARs are highlighted while utilizing the body tissues presentation from the CT scans.

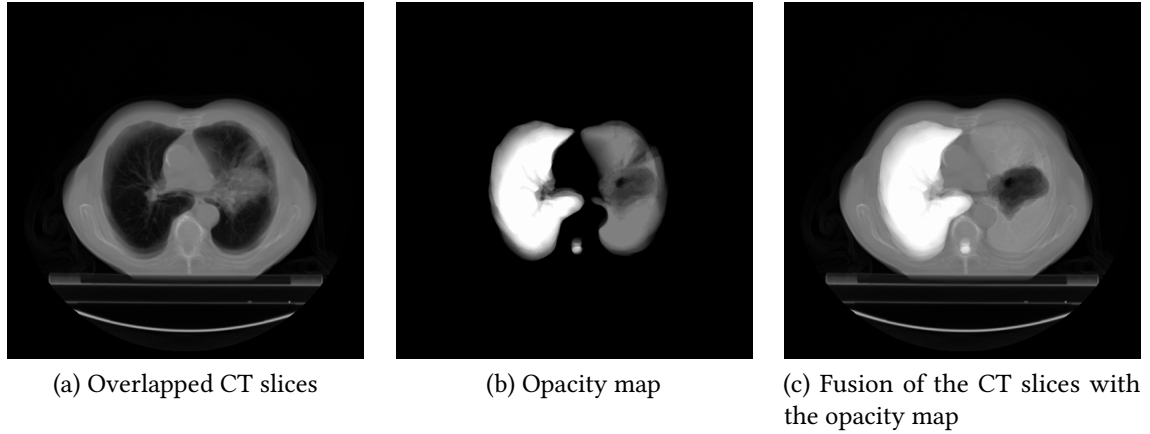


Figure 32: Fusion process where CT slices are blended with the opacity map.

Algorithm 3 Opacity calculation

Input: $images[N, W, H] | N > 0, W > 0, H > 0$,
 where $images$ are the CT images that contain the tumor, N is the total number of the mentioned CT images, and W and H are their width and height.

Output: Array $opacity[0 \cdots W - 1, 0 \cdots H - 1]$

```

 $opacity \leftarrow [0 \cdots 0, 0 \cdots 0]$  ▷ Init with black color
 $ops \leftarrow 1/N$  ▷ Opacity per layer
for  $n \leftarrow 0$  to  $N - 1$  do ▷ Handle OARs
  for  $w \leftarrow 0$  to  $W - 1$  do
    for  $h \leftarrow 0$  to  $H - 1$  do
      if  $images[n, w, h] \in OAR$  then
        if  $OAR \cap tumor$  then
           $opacity[w, h] \leftarrow opacity[w, h] + 0.5 * ops$ 
        else
           $opacity[w, h] \leftarrow opacity[w, h] + 1 * ops$ 
        end if
      end if
    end for
  end for
end for

for  $n \leftarrow 0$  to  $N - 1$  do ▷ Handle tumor
  for  $w \leftarrow 0$  to  $W - 1$  do
    for  $h \leftarrow 0$  to  $H - 1$  do
      if  $images[n, w, h] \in tumor$  then
         $opacity[w, h] \leftarrow 0$ 
      end if
    end for
  end for
end for
  
```

To perform beam discovery, Algorithm 4, which evaluates the beam's accumulated color, was employed. Since the CT images contain noise, the fusion image must have been picking it up. Hence, a threshold is needed, but this is not a must, as it depends on how the beams' color is evaluated. The output of Algorithm 4 after being processed is illustrated in Figure 33. The pink tumor centroid is the origin of the beams. Since the angle discovery is performed in 2D, it is fast and reproducible. As shown, the algorithm is capable of avoiding OARs, which are the right lung and the spinal cord. The red, yellow, green, and purple lines represent 0° , 90° , 180° , and 270° , respectively. This follows the convention that was specified in Section 2.2.2.

Algorithm 4 Beam color calculation

Input: $image[W, H]$ | $W > 0, H > 0$,
 $beam_origin(x, y)$
 $threshold$

where $image$ is the fusion image, and W and H are the width and height of it; $beam_origin(x, y)$ is the (x, y) coordinates of the ray origin, and $threshold$ is used to filter noise.

Output: Array $angles[0 \dots 359]$

$angles \leftarrow [0 \dots 0]$

▷ Init with black color

for $w \leftarrow 0$ to $W - 1$ **do**

for $h \leftarrow 0$ to $H - 1$ **do**

if $average(image[w, h]) < threshold$ **then**
 skip

end if

$\varphi \leftarrow \angle(beam_origin, (w, h))$

▷ Calculate the angle

$angles[\varphi] \leftarrow angles[\varphi] + image[w, h]$

end for

end for

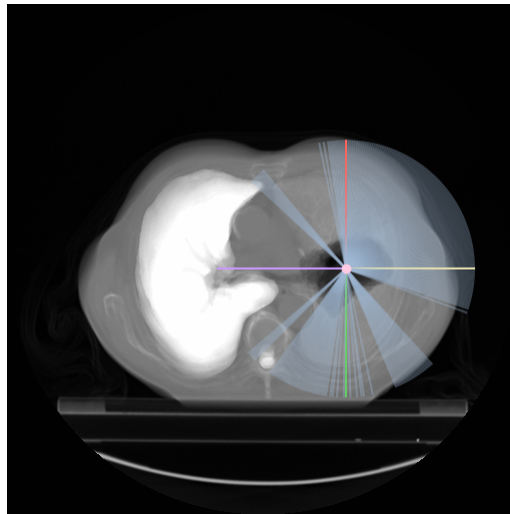


Figure 33: Angle discovery is capable of avoiding OARs while targeting GTV.

At first glance, the ranges $[110^\circ, 140^\circ]$, $[150^\circ, 170^\circ]$, and $[320^\circ, 350^\circ]$ were not accepted as abnormal as they seem to have good positions. However, the algorithm is working as it should since we want to minimize the dose to healthy tissue and maximize it to the tumor. If those angles had been accepted, the targeted tumor area would have been much smaller than the irradiated left lung area.

One important finding is that a good angle returned by this angle discovery step does not necessarily mean it is ultimately selected. This can be explained by using Figure 34. The tumor, whose color is purple, and the gantry trajectory are simplified as circles whose centers are notated by O . The OARs are represented by the two pink circles. A blue angle \widehat{BOC} with the angle value α , where the radiation beams originated from O are not blocked by OARs, is assumed to exist. On the circular arc \widehat{BC} , point A is selected as a candidate for beam position. From there, radiation beams can be emitted within an upper limit α -angle. By assuming that the IMRT has only one field represented by the green angle β , this field has to cover as much area of the GTV as possible. While the OAR_2 is outside of the beam, the OAR_1 is irradiated.

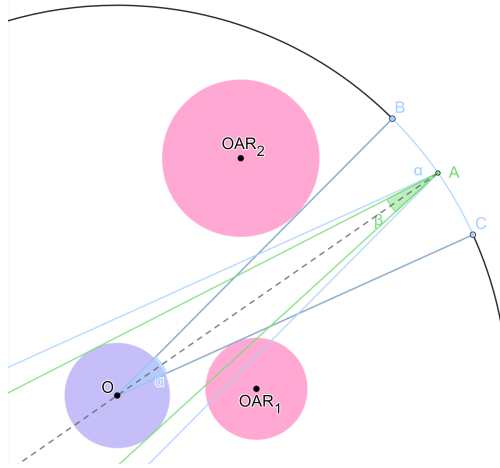


Figure 34: Illustration of upper limit α -angle.

4.2.2 Angle selection

After getting good gantry angle ranges, the next step is to select individual angles based on the given number of fields. K-means clustering was chosen, as it can correctly return the number of clusters as required. Since the angles are in degrees and there is a discontinuous in the value, which is value 359° and 0° , the angles have to be transformed so that Euclidean distance can be calculated, and the discontinuous is mitigated. Hence, the conversion is performed by using:

$$\begin{aligned} x &= \sin(\text{angle}) \\ y &= \cos(\text{angle}). \end{aligned} \tag{17}$$

where *angle* is the angle that needs to be converted and (x, y) is the converted Cartesian coordinates. By using *sin* and *cos* for x and y , respectively, the convention in Section 2.2.2, which is the angle starts from straight vertical and rotates clockwise, is followed.

As an example, the output of K-means clustering for the good gantry angle ranges of patient LUNG1-001 is represented in Figure 35.

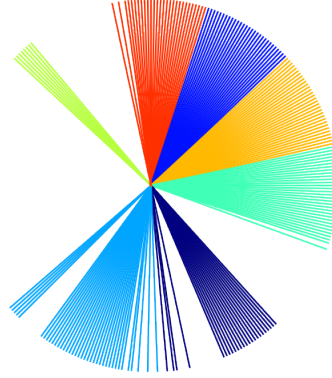


Figure 35: Clusters of good gantry angle ranges of patient LUNG1-001.

As mentioned in Section 2.2.7, if the beams are too close, the dose can sum up. Hence, a good strategy, for now, is to select the middle angle of the clusters. By doing this, the distance between the angles can be ensured. If there is a gap in the cluster, such as the dark purple cluster in Figure 35, and the precise middle angle does not exist, the closest one might be a good alternative. Figure 36 illustrates the middle angles in black, which are also the gantry angles for the IMRT plan.

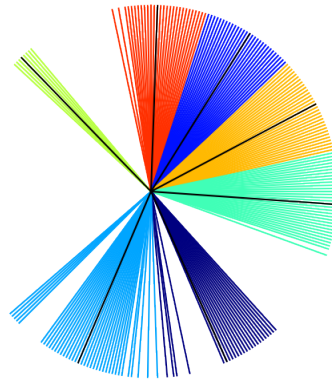


Figure 36: Gantry angles are chosen from the given clusters.

As the K-means clustering was performed solely based on the beam geometry, it is hard to determine whether the task was performed well. However, as the angle 359° and 0° were partitioned into the same cluster, the conversion performed by Equation 17 worked. Besides visually assessing the clustering quality, evaluation metrics were calculated. For K-means clustering targeting seven clusters, the Silhouette index ranges from 0.52 to 0.65 with a mean of 0.56 and a standard deviation of 0.03, while the Davies-Bouldin index ranges from 0.38 to 0.55 with a mean of 0.48 and a standard deviation of 0.04.

5 Evaluation

This section will evaluate the performance of the reverse beam method. The IMRT plans generated by the proposed method will be compared against the IMRT plans with seven equidistant fields. Furthermore, a more sophisticated method to select gantry angles from given clusters will be introduced, and ideas for future work will be suggested.

5.1 Performance

The run time of the fusion and color calculation algorithms is listed in Appendix A. In general, if the CT scan size varies, the run time is expected to be $O(nk^2)$ and $O(k^2)$ where k is the CT slice dimensions and n is the number of CT slices. Assuming the CT scans have the same size, the expected run time of the fusion and color algorithms are $O(n)$ and $O(1)$, respectively. Table 3 shows the statistics of the angle discovery algorithm and Figure 37 plots the fusion algorithm run time. The following values are reported as mean \pm standard deviation. In general, each patient has 21.2 ± 9.7 CT slices, and 4.4 ± 0.8 OARs. The fusion and color calculation tasks took 8.9 ± 4.7 s and 1.6 ± 0.1 s to complete, respectively.

Patient	No. CT slices	No. OARs	Fusion time (s)	Color cal. time (s)
LUNG1-017	43	4	21.1	1.5
LUNG1-019	19	4	8.5	1.9
LUNG1-026	48	5	20.4	1.6
LUNG1-027	3	3	1.0	1.7
LUNG1-032	27	4	10.4	1.3

Table 3: Angle discovery statistics.

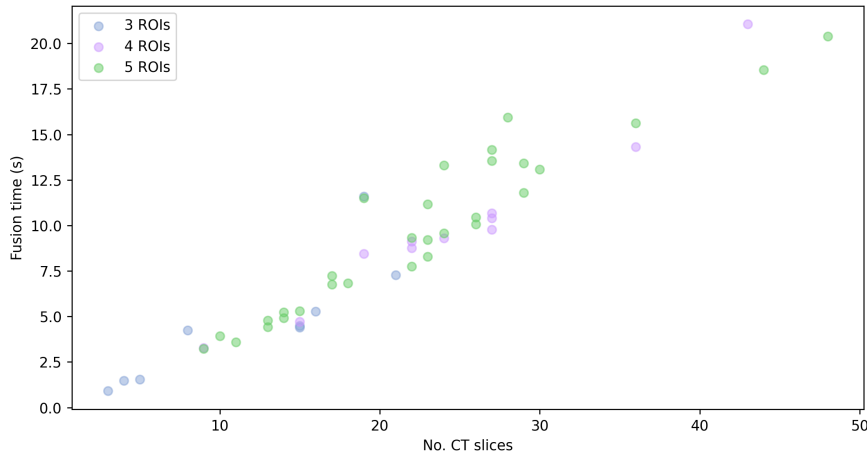


Figure 37: Fusion time has a strong correlation (0.952) with the number of CT slices.

Figure 38 illustrates how often an angle was returned by the angle discovery algorithm. The Jet colormap is used to represent the angle distributions, which means the red color angles are selected more often than the blue ones. The white and black lines represent the angles that appear the most (the first occurrence) and the least (the first occurrence), respectively. In general, it can be seen that the algorithm favors the angles that were not blocked by the lungs. The exhausted list of the angle probability can be found in Appendix B.

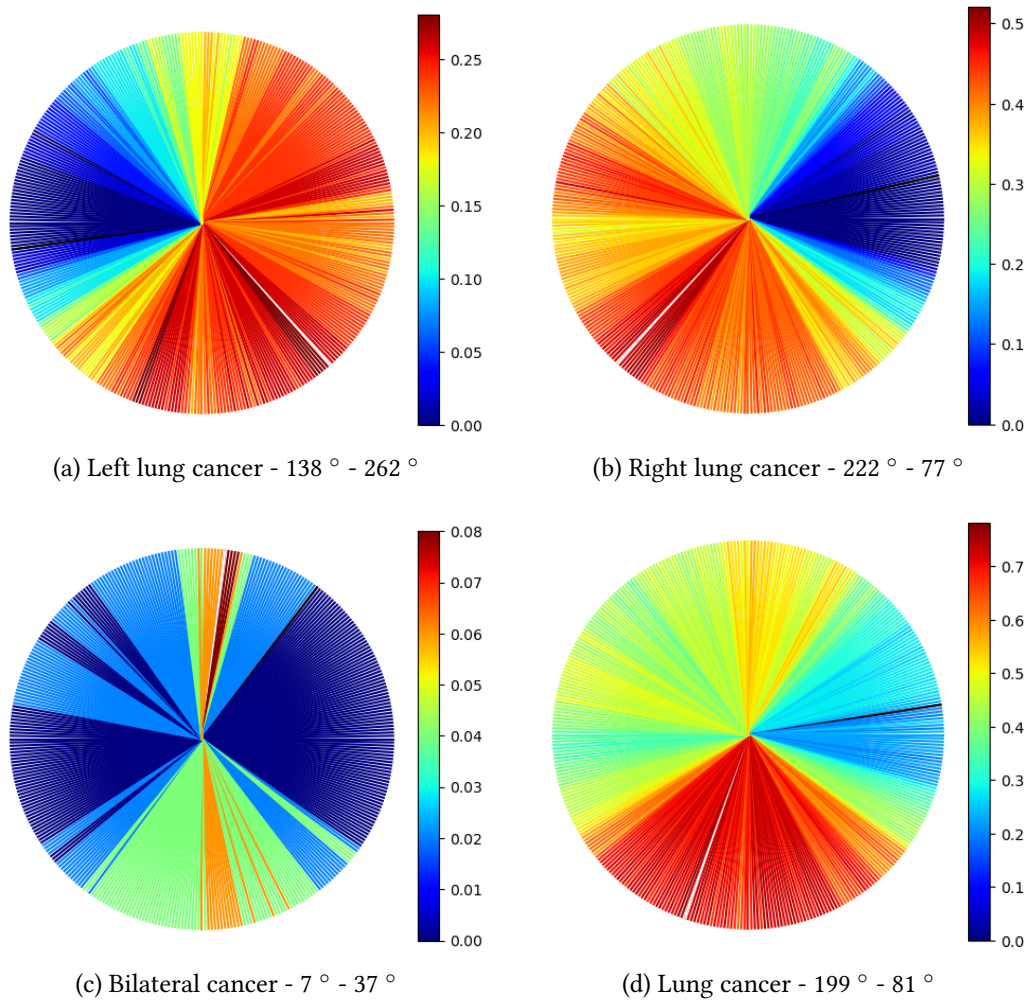


Figure 38: Output of the angle discovery algorithm.

5.2 Comparison

Via clinical goals, which were described in Table 1, the plans generated by the reverse beam method are compared against the ones with equidistant fields. All plans are IMRT plans with seven fields with 45° collimator rotations generated by Ethos therapy system. In short, both methods have their advantages and disadvantages.

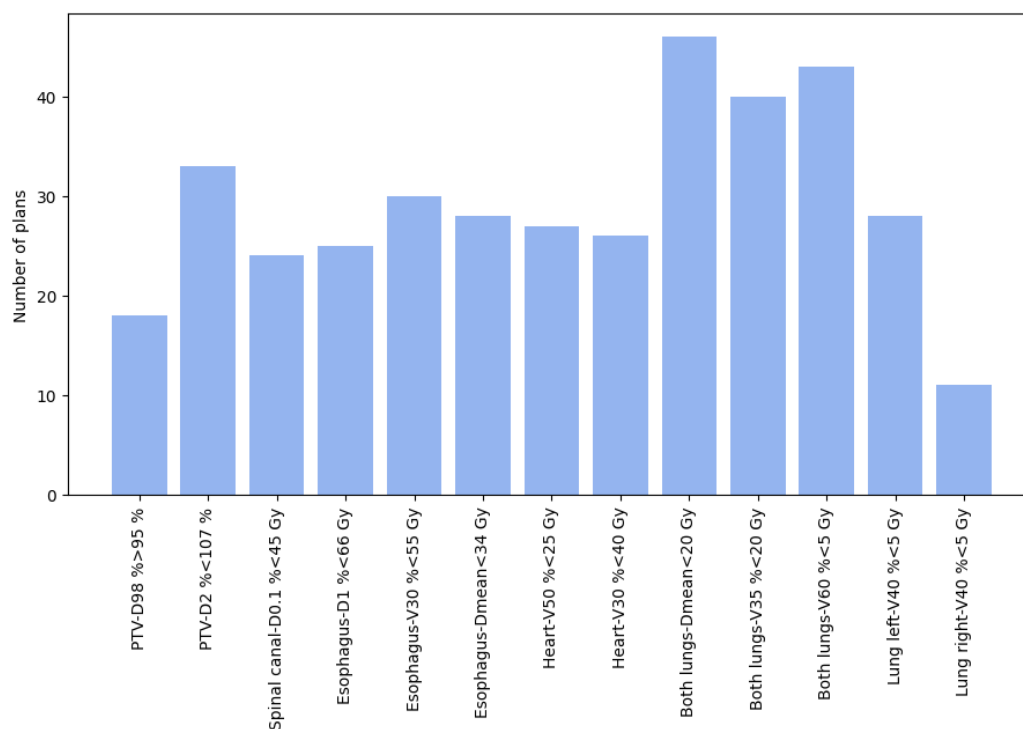


Figure 39: Clinical goals that the reverse beam method performed better.

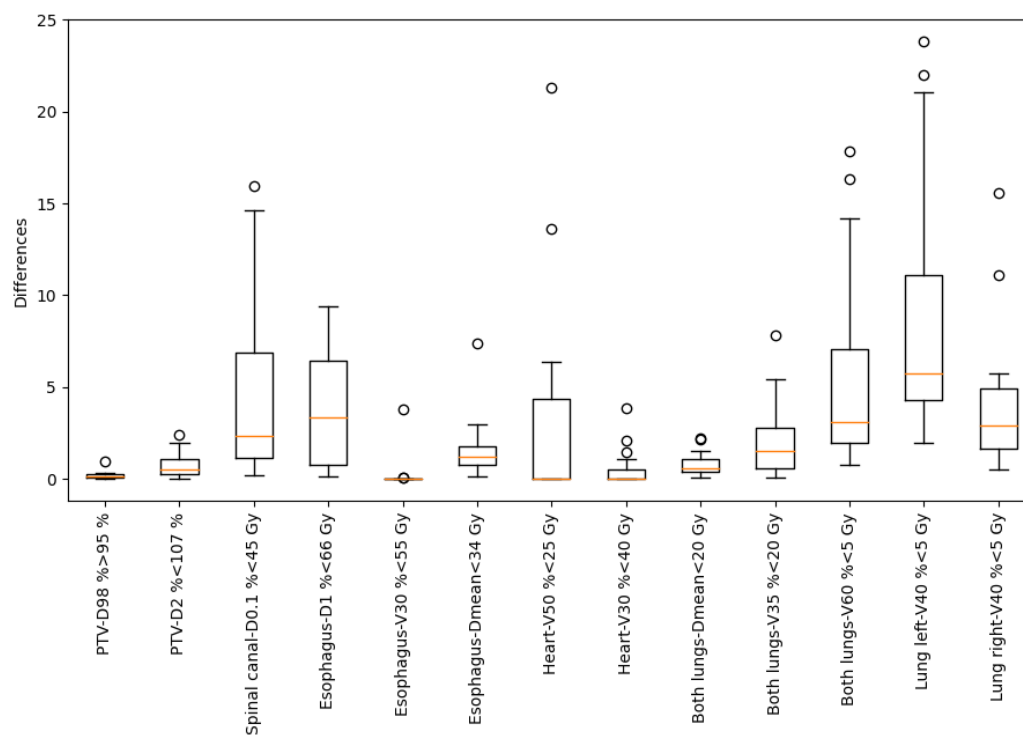


Figure 40: Clinical goals that the reverse beam method performed better.

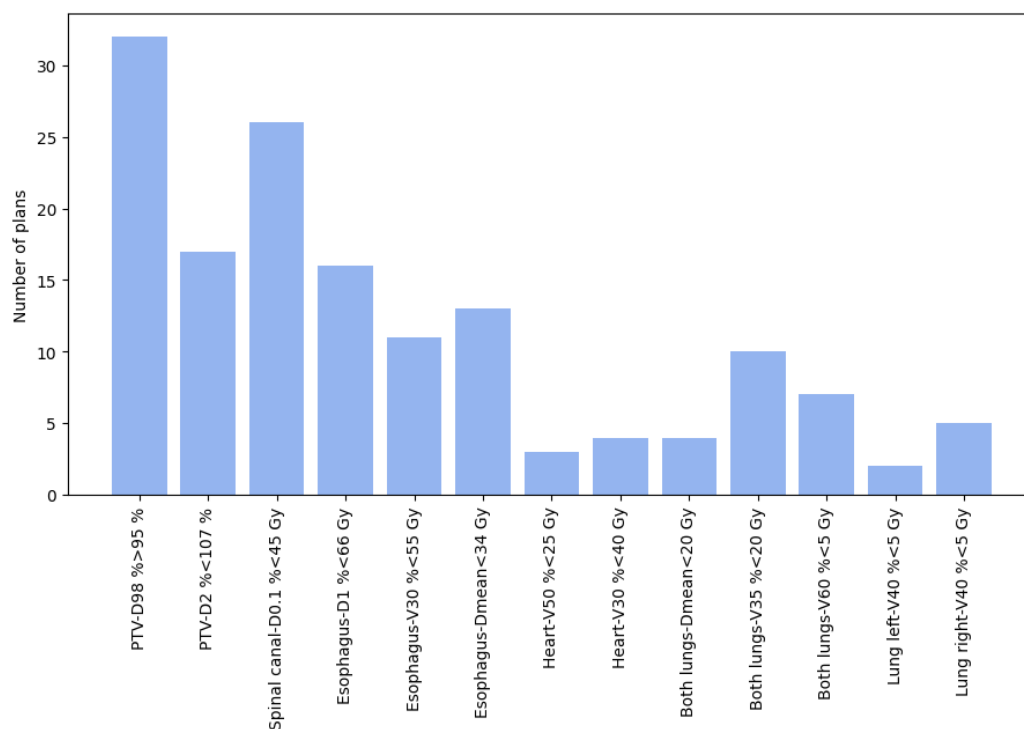


Figure 41: Clinical goals that the reverse beam method performed worse.

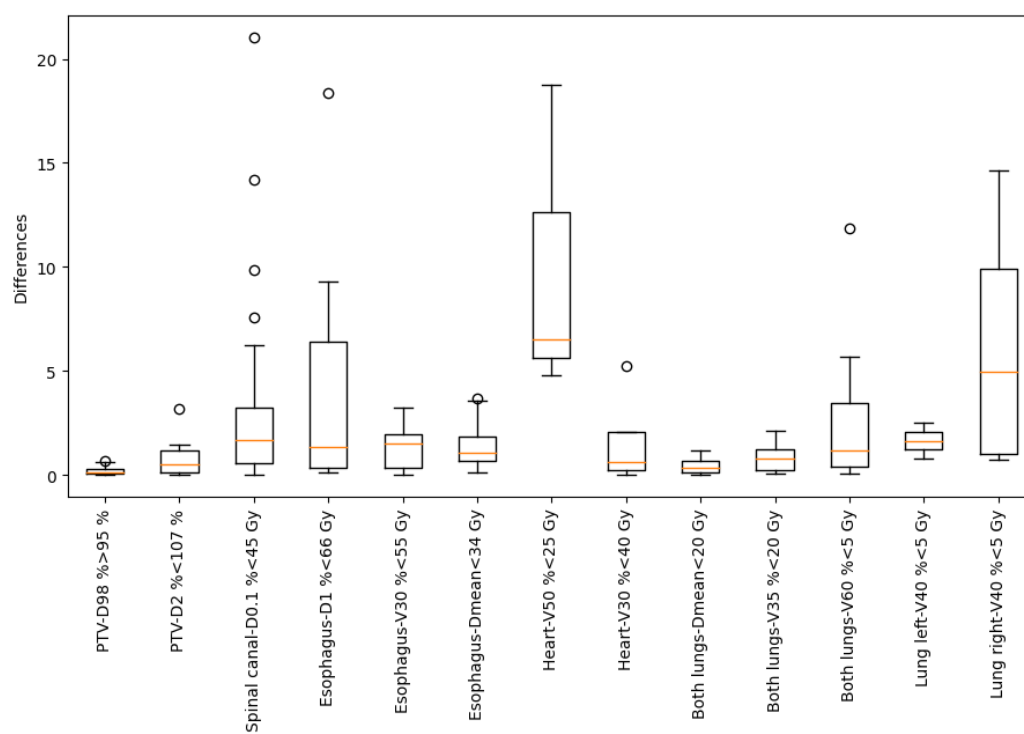


Figure 42: Clinical goals that the reverse beam method performed worse.

As shown in Figure 39, for 50 patients, the reverse beam method performs well in avoiding irradiating the lungs, heart, and esophagus, which is expected and explainable. Figure 40 illustrates the difference between the two types of plans in terms of clinical goals. There are outliers in the heart goal, as not all patients have the heart contoured.

Taking patient LUNG1-001 as an example, Figure 43 illustrates the angles of an IMRT plan with seven equidistant fields in green and the angles of an IMRT plan generated by the reverse beam method in blue. The selected angles are 32° , 65° , 98° , 158° , 205° , 316° , and 357° . One of the Ethos plan beams goes straight through the right lung while the reverse beam method avoids it, which leads to the advantages. The clinical goals comparison is also shown in Table 4, which reflects the observation from Figure 40.

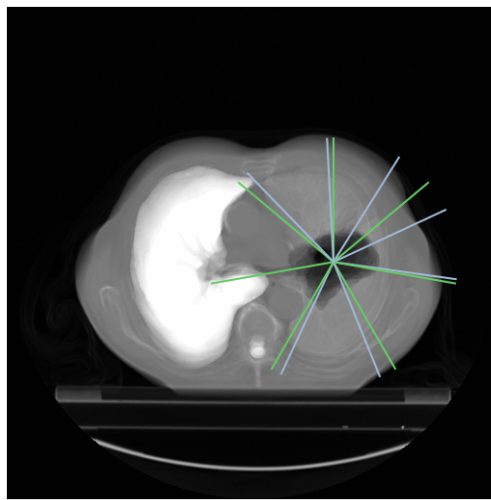


Figure 43: The gantry angles returned by the reverse beam method and the equidistant angles are in blue and green, respectively - LUNG1-001.

ROI	Clinical goals			Equidistant fields	Reverse beam
PTV	D98.0 %	>	95.0 %	95.3 %	95.2 %
	D2.0 %	<	107.0 %	104.6 %	103.9 %
Spinal canal	D0.1 %	<	45.0 Gy	22.74 Gy	22.00 Gy
Both lungs	Dmean	<	20.0 Gy	10.18 Gy	9.35 Gy
	V20.0 Gy	<	35.0 %	17.9 %	16.9 %
	V5.0 Gy	<	60.0 %	40.3 %	33.9 %
Lung right	V5.0 Gy	<	40.0 %	31.9 %	20.8 %

Table 4: Comparison between the plans with equidistant fields and with the fields returned by the reverse beam method - LUNG1-001.

Similarly, it can be seen from Figure 41 and Figure 42 that the reverse beam method performs badly for the spinal canal. Even though the goal PTV D98.0 % > 95.0 % looks bad at the first glance, it is still acceptable as the difference between the two types of plans is not much, which can be observed from Figure 42.

Patient	Silhouette index	Davies–Bouldin index
LUNG1-001	0.61	0.44
LUNG1-010	0.57	0.47
LUNG1-013	0.55	0.50
LUNG1-017	0.61	0.48
LUNG1-033	0.60	0.45

Table 5: Evaluation metrics of K-means clustering outputs.

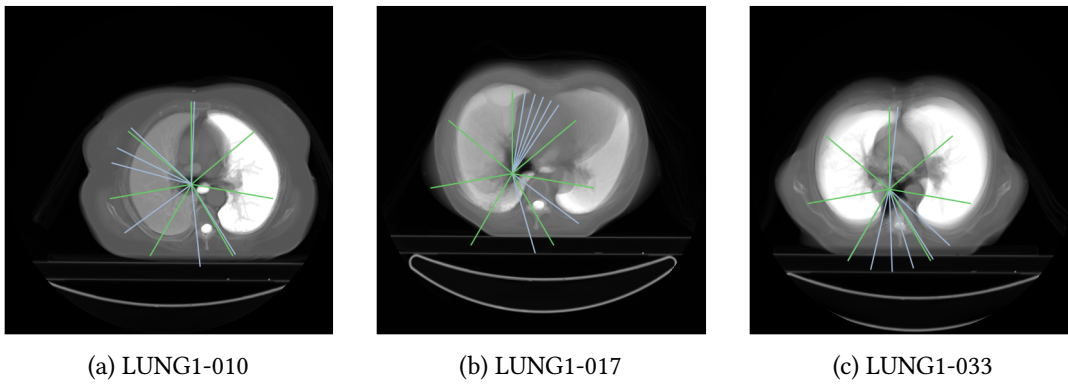


Figure 44: Poor performance for bilateral cancer patients. The gantry angles returned by the reverse beam method and the equidistant angles are in blue and green, respectively.

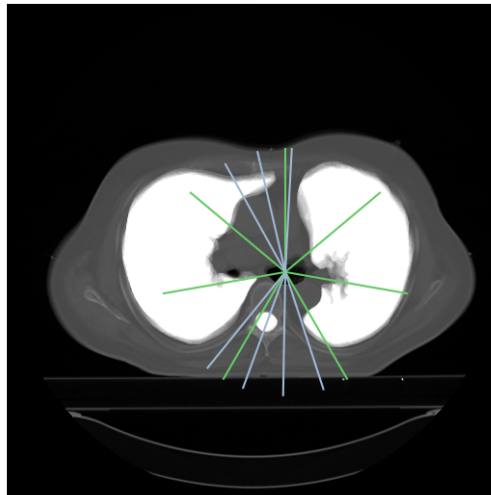


Figure 45: The gantry angles returned by the reverse beam method and the equidistant angles are in blue and green, respectively - LUNG1-013.

ROI	Clinical goals			Equidistant fields	Reverse beam
PTV	D98.0 %	>	95.0 %	95.2 %	95.2 %
	D2.0 %	<	107.0 %	103.5 %	106.7 %
Spinal canal	D0.1 %	<	45.0 Gy	21.91 Gy	42.93 Gy
Both lungs	Dmean	<	20.0 Gy	3.48 Gy	2.04 Gy
	V20.0 Gy	<	35.0 %	1.6 %	2.5 %
	V5.0 Gy	<	60.0 %	21.5 %	8.3 %

Table 6: Comparison between the plans with equidistant fields and with the fields returned by the reverse beam method - LUNG1-013.

While plans for bilateral cancer have relatively good evaluation metrics compared to LUNG1-001 as shown in Table 5, it can be confirmed that the algorithm does not perform well for bilateral cancer, as three out of four plans generated by the reverse beam method perform worse than the ones with equidistant fields. Figure 44 illustrates the selected gantry angles compared to seven equidistant fields for patients that have bilateral cancer: LUNG1-010, LUNG1-017, and LUNG1-033, besides LUNG1-013. Patient LUNG1-013, whose tumor locates outside both of the lungs as shown in Figure 45, is used as an example of an unexpected study case causing the 20 Gy outlier for the spinal canal clinical goal. The selected angles are 3°, 162°, 181°, 200°, 219°, 331°, 347°. The clinical goals comparison is also shown in Table 6. Since the good angle ranges for the beams are narrowed, the algorithm incorrectly selects an angle that goes through the spinal canal. Additionally, a part of the right lung is also impacted. This behavior is understandable, as the spinal canal and the affected part of the lung are smaller than the rest of the lungs, the algorithm chose the angles that have the least impact as sacrificing healthy tissue is unavoidable in this situation.

5.3 Ranking angles

Instead of choosing the middle angle from a given range as described in Section 4.2.2, a more sophisticated method was explored. By leveraging the fluctuation of the MU⁴³, the angles inside a cluster were ranked accordingly. Better gantry angles were found and the total number of beams was lowered by consolidating closely distanced angles. Unfortunately, this method is impractical as it is resource-demanding. Patients LUNG1-001 and LUNG1-013 were used for evaluation.

5.3.1 Observations

The RTPD dataset was used to observe the relation between MU and good gantry angles. Given an IMRT plan with 12 equidistant fields and 12 IMRT plans with 1 field whose gantry angle belongs to the given 12 equidistant fields:

⁴³BeamMeterset - Tag (300A,0086)

$$\begin{aligned}
W_i &= \frac{MU_i}{\sum_{n=1}^{12} MU_n} \\
W_{12_i} &= \frac{MU_{12_i}}{\sum_{n=1}^{12} MU_{12_n}} \\
S_i &= W_i - W_{12_i},
\end{aligned} \tag{18}$$

where S_i is the score of the angle i , W_i and W_{12_i} are the weight of the angle i of the IMRT plans with one field and 12 equidistant fields, respectively, MU_i is the monitor unit of the angle i from the IMRT plan with one field and MU_{12_i} is the monitor unit of the angle i from the IMRT plan with 12 equidistant fields.

Corollary 5.1 *The proposed gantry angle ranges are constrained by OARs, but not obstructed by them. Hence, the difference between the weights W_i and W_{12_i} represented by the score S_i relates solely to the body tissue.*

By comparing the score S_i , with Corollary 5.1 and the definition of MU mentioned in Section 2.2.6, Lemma 5.1 can be made:

Lemma 5.1 *If the score S_i is non-negative, i.e. the weight W_i is greater than or equal to the weight W_{12_i} , the angle i must be a good gantry angle as more dose can be delivered to the same tumor volume without affecting surrounding OAR(s).*

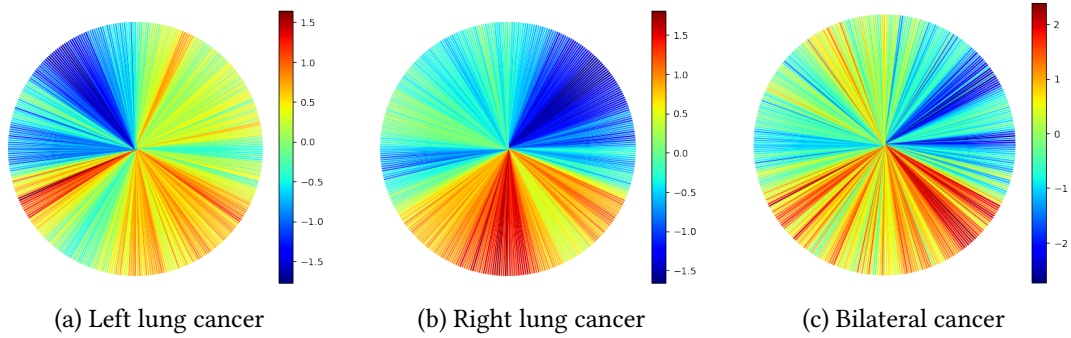


Figure 46: The scores of the angles were calculated by using Equation 18.

The scores of the angles illustrated by Figure 46 are fairly in alignment with Figure 38 illustrating how often an angle was returned by the angle discovery algorithm. The Jet colormap is used to represent the scores of the angles, which means the red color angles have higher scores than the blue ones. Additionally, by ranking the gantry angles based on their score S , it is highly likely that there exist adjacent clusters where the angles with the highest score are closely distanced. Since the doses from closely distanced angles accumulated as mentioned in Section 2.2.7, these angles can be consolidated resulting in a lower-than-required number of beams. For experimental purposes, 15° is the threshold value that was used to define the close distance. Furthermore, any beam angles that have a negative score will also be eliminated.

5.3.2 Result

Figure 47 and Figure 48 illustrate the scores by using the Jet color scheme. The color can be interpreted as if the score of a gantry angle is higher than the scores of other angles in the same cluster, the red color will be used.

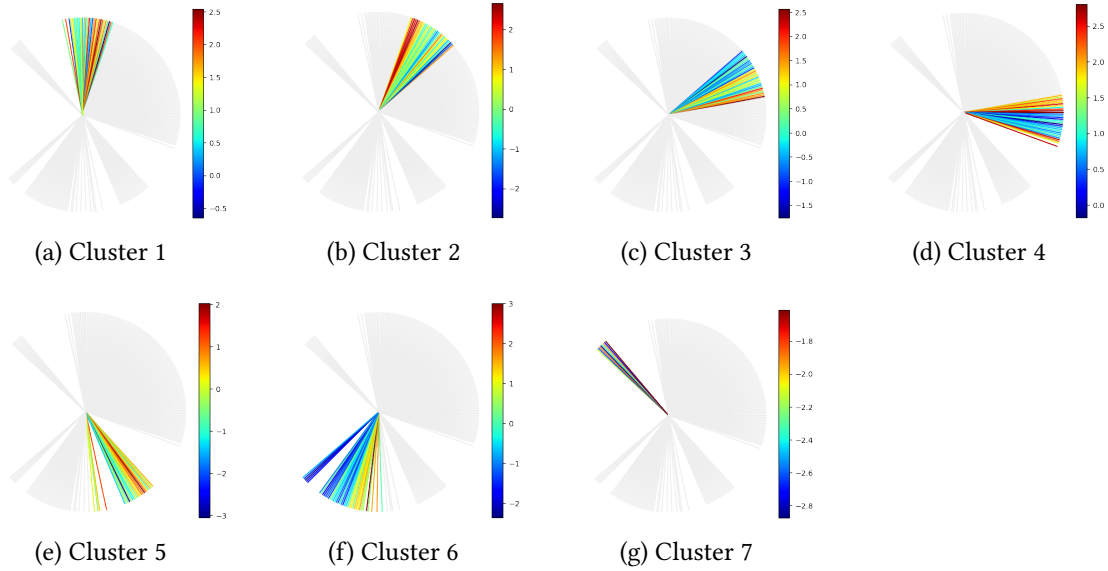


Figure 47: Scores of the angles - LUNG1-001.

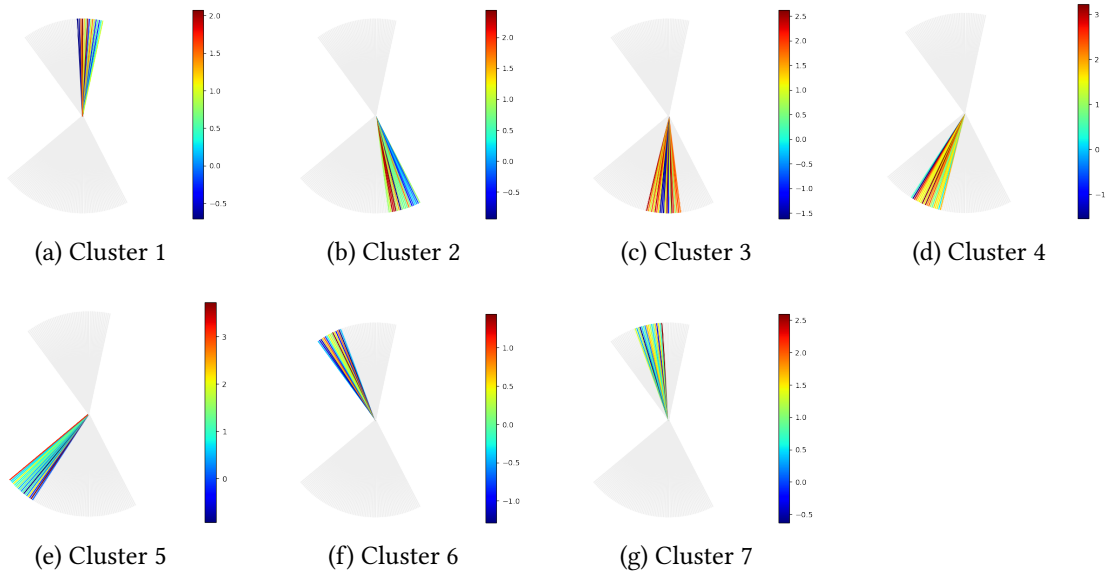


Figure 48: Score of the angles - LUNG1-013.

As observed in Figure 47 and Figure 48, the scores can be positive, negative, or zero. This is presented by Figure 49 where the blue color is used for angles whose score is non-negative, and the grey color stands for the rest.

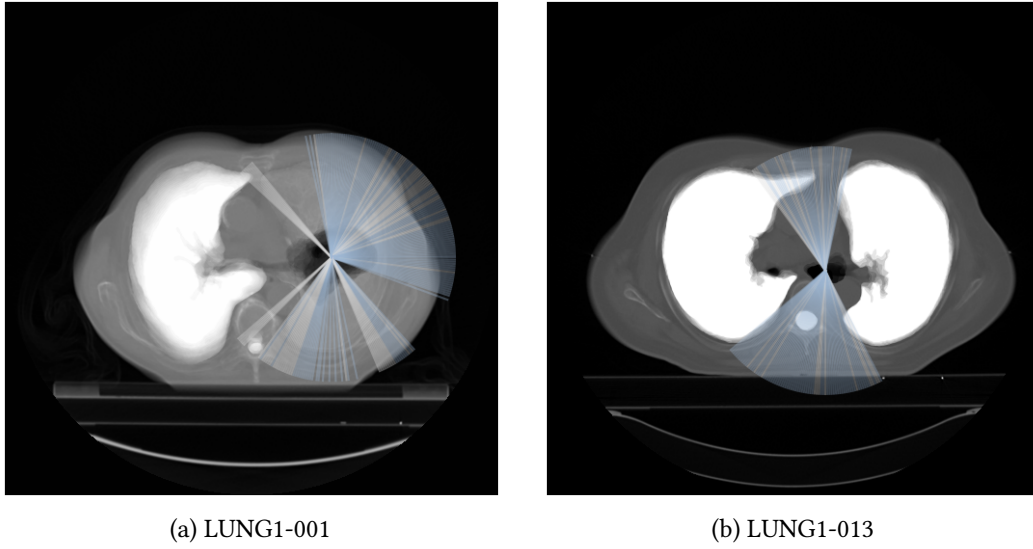


Figure 49: Angles that have non-negative scores are in blue.

LUNG1-001		LUNG1-013	
Angle	Score	Angle	Score
11°	2.5	0°	2.1
23°	2.7	168°	2.4
79°	2.6	178°	2.6
90°	2.8	205°	3.2
144°	2.0	214°	3.7
187°	3.0	334°	1.4
320°	-1.6	356°	2.6

Table 7: The angles that have the highest scores in each cluster of the seven clusters.

In each cluster, the angle whose score is highest will be selected. Table 7 shows the angles that have the highest score in each cluster of the seven clusters from patients LUNG1-001 and LUNG1-013. For patient LUNG1-001, the most suitable angles are 11°, 23°, 79°, 90°, 144°, 187°, 320°, with the angles 11°, 79°, and 320° removed. Hence, this results in an **IMRT plan with four fields**. In regards to patient LUNG1-013, the good angles are 0°, 168°, 178°, 205°, 214°, 334°, 356°, with the angle 0°, 168°, 205° removed. As a result, an **IMRT plan with four fields** was created.

To perform an exhaustive comparison, IMRT plans with four fields were generated by using the original reverse beam method with the middle angles selected. The middle angles are 76°, 156°, 203°, and 357° for patient LUNG1-001; and 0°, 172°, 211°, and 335° for patient LUNG1-013. Additionally, IMRT plans with four equidistant fields were also created for completeness. Figure 50 illustrates the angles of an IMRT plan with seven equidistant fields in blue, the angles of an IMRT plan with four equidistant fields in green, the angles of an IMRT plan with four fields generated by the original reverse beam

method in yellow, and the angles of an IMRT plan with four fields and ranked angles in purple.

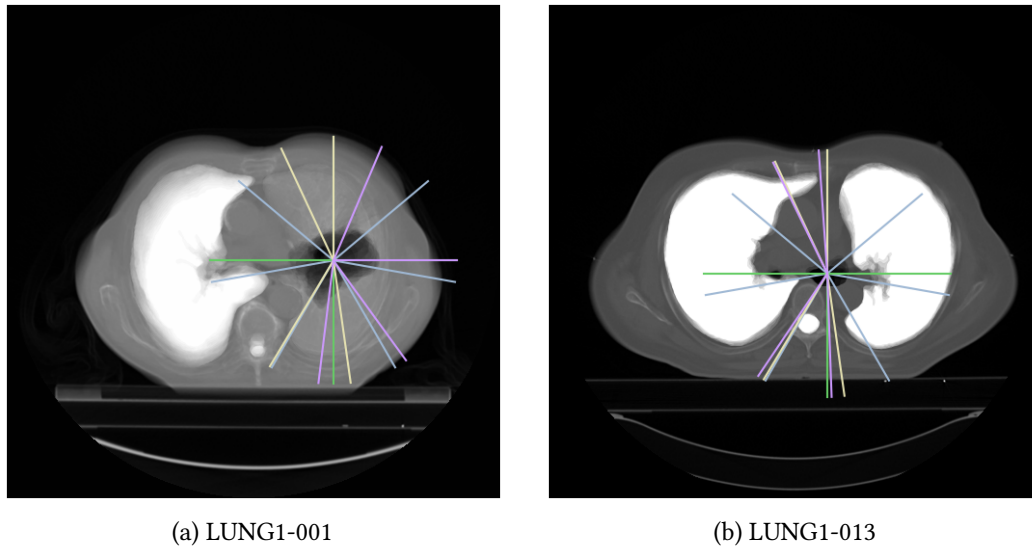


Figure 50: The angles of an IMRT plan with seven equidistant fields are blue, the angles of an IMRT plan with four equidistant fields are green, the angles of an IMRT plan with four fields generated by the original reverse beam method are yellow, and the angles of an IMRT plan with four fields and ranked angles are purple.

ROI	Clinical goals		7 e. f. ¹	4 e. f. ²	M. a. ³	R. a. ⁴
PTV	D98.0 %	> 95.0 %	95.3 %	95.2 %	95.1 %	95.2 %
	D2.0 %	< 107.0 %	104.6 %	105.7 %	105.1 %	105.6 %
Spinal canal	D0.1 %	< 45.0 Gy	22.74 Gy	2.21 Gy	22.76 Gy	14.72 Gy
Both lungs	Dmean	< 20.0 Gy	10.18 Gy	11.17 Gy	9.75 Gy	9.66 Gy
	V20.0 Gy	< 35.0 %	17.9 %	22.2 %	15.8 %	14.7 %
	V5.0 Gy	< 60.0 %	40.3 %	36.9 %	34.8 %	37.0 %
Lung right	V5.0 Gy	< 40.0 %	31.9 %	27.5 %	22.5 %	26.5 %

- 1 IMRT plan with seven equidistant fields.
- 2 IMRT plan with four equidistant fields.
- 3 IMRT plan with four fields generated by the original reverse beam method with the middle angles selected.
- 4 IMRT plan with four fields generated by the reverse beam method with ranked angles.

Table 8: Comparison between different IMRT plans - LUNG1-001.

ROI	Clinical goals			7 e. f. ¹	4 e. f. ²	M. a. ³	R. a. ⁴
PTV	D98.0 %	>	95.0 %	95.2 %	95.1 %	95.0 %	95.3 %
	D2.0 %	<	107.0 %	103.5 %	103.6 %	105.2 %	104.3 %
Spinal canal	D0.1 %	<	45.0 Gy	21.91 Gy	42.34 Gy	43.86 Gy	44.36 Gy
Both lungs	Dmean	<	20.0 Gy	3.48 Gy	2.91 Gy	1.85 Gy	2.06 Gy
	V20.0 Gy	<	35.0 %	1.6 %	4.7 %	1.8 %	2.1 %
	V5.0 Gy	<	60.0 %	21.5 %	11.8 %	7.0 %	8.1 %

- 1 IMRT plan with seven equidistant fields.
- 2 IMRT plan with four equidistant fields.
- 3 IMRT plan with four fields generated by the original reverse beam method with the middle angles selected.
- 4 IMRT plan with four fields generated by the reverse beam method with ranked angles.

Table 9: Comparison between different IMRT plans - LUNG1-013.

Table 8 and Table 9 compare the clinical goals between different plans of patients LUNG1-001 and LUNG1-013, respectively. Even though this method still does not perform well on bilateral cancer, the results of patient LUNG1-001 are acceptable with all clinical goals passed. Furthermore, when lowering the number of fields for patient LUNG1-013, with the original reverse beam method, one clinical goal failed while with ranked angles, the same goal passed. It can be concluded that by ranking angles, clinical goals can be achieved and the number of fields can be even lowered.

5.4 Future development

The proposed reverse beam method has been focused only on the coplanar IMRT plans where the couch does not rotate. To support non-coplanar plans, 3D transformations, which were mentioned in Section 2.3.2, can be applied at the beginning of the workflow to rotate the structure set accordingly. However, another problem might arise, that is how to create a fusion image properly from skewed images.

As mentioned in Section 4.2.1, the z -value truncation caused data loss. So far, the used dataset has regularly shaped tumors with an assumption that the tumor mass is equally distributed. In case the tumor is too long leading to multiple pseudo-centroids, the proposed method will not work well as not all tumor surfaces can be irradiated. Instead of creating a fusion image for all layers at once, multiple fusion images can be created.

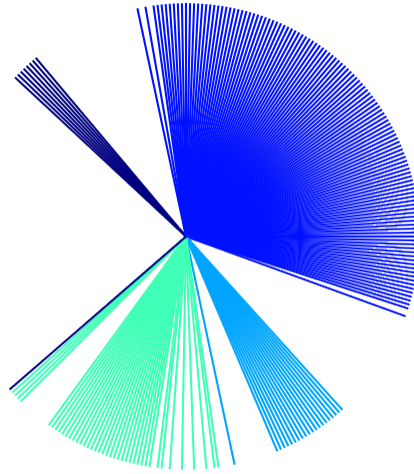


Figure 51: Clustering using HDBSCAN and the haversine distance - LUNG1-001.

As discussed in Section 4.2.2, the angle clustering is performed by using the K-means algorithm. While testing against HDBSCAN⁴⁴ using the haversine distance, a good clustering result was also achieved as seen in Figure 51. The Silhouette index ranges from 0.02 to 0.80 with a mean of 0.42 and a standard deviation of 0.17. The Davies-Bouldin index ranges from 0.29 to 12.69 with a mean of 1.09 and a standard deviation of 1.75. This approach might be useful when finding a plan that has as few beams as possible.

Last but not least, the ranking angles method proposed in Section 5.3 is impractical as it requires too many plans to be generated. Given specific constraints, if there exists a deep learning model that can predict the MU efficiently, the proposed improvement might become realistic. Additionally, the angles are clustered solely based on the geometry. Perhaps clustering based on MU from the beginning might yield a good result as stated in Lemma 5.1.

⁴⁴<https://hdbscan.readthedocs.io/en/latest/>

6 Conclusions

The primary goal of this thesis was to find good gantry angles for IMRT plans by combining computer graphics and machine learning. In this work, a new method called *reverse beam* was introduced to aid the plan generation process. The proposed solution consists of two stages: angle discovery and angle selection. In the first stage, an algorithm to fuse CT images by leveraging the opacity map was employed. Based on the fusion output, an algorithm inspired by ray casting performs an evaluation to find good angle ranges. In the second stage, K-means clustering algorithm is responsible to partition the angles based on their geometry. Finally, good distanced angles are chosen from the processed clusters.

Through testing and validation, this thesis has successfully answered the three research questions that were made at the beginning of the work. For the first question "How well does the proposed method perform, in terms of performance and quality ?", the algorithms illustrated good performance as they are capable of avoiding organs while targeting tumors in an acceptable time frame. The second question "How do the new plans compare to the ones with equidistant fields ?" was answered by using IMRT plans with seven equidistant fields with 45° collimator rotations generated by Ethos as a baseline. The reverse beam method performs better while preserving the organs from radiation as the gantry angles are personalized instead of being hard-coded. For the last question "Is there an IMRT plan that has fewer beams than the given one, but is still capable of achieving the same clinical goals ?", the answer is yes. By ranking the angles based on the MU, the number of beams was proven to be lower-able while achieving predefined clinical goals.

While this thesis demonstrated how ray casting and K-means clustering algorithm can be used together to find good gantry angles, there is still room for improvement. For example, while the plans generated by the reverse beam method for bilateral cancer passed the given clinical goals, they can still be refined. Furthermore, the reverse beam method was evaluated by comparing clinical goals. A more sophisticated method that employs dose distribution comparisons might yield better insights into how homogeneous the doses are.

In conclusion, radiation therapy is complex and radiotherapy treatment planning is more than just optimizing the beam geometry. Defeating cancer is not a battle that can be won in just one day and may need many generations to come. In the meantime, raising cancer awareness and participating in screening programs might keep cancer incidence in control. By investing in research, the discovery of more advanced treatment methods can be accelerated. With that being said, the author believes that ultimately, this thesis work will contribute to the creation of a world without fear of cancer.

References

- [1] World Health Organization, “Cancer,” 2022, <https://www.who.int/health-topics/cancer>. Accessed 11.11.2022.
- [2] Global Cancer Observatory, “All cancers,” <https://gco.iarc.fr/today/data/factsheets/cancers/39-All-cancers-fact-sheet.pdf>. Accessed 11.11.2022.
- [3] S. McDowell, S. L. Rausch, and K. Simmons, “Cancer Research Insights from the Latest Decade, 2010 to 2020,” 2019, <https://www.cancer.org/latest-news/cancer-research-insights-from-the-latest-decade-2010-to-2020.html>. Accessed 29.04.2023.
- [4] National Cancer Institute, “Annual Report to the Nation 2022: Overall Cancer Statistics,” https://seer.cancer.gov/report_to_nation/statistics.html. Accessed 29.04.2023.
- [5] American Cancer Society, “How Radiation Therapy Is Used to Treat Cancer,” 2019, <https://www.cancer.org/treatment/treatments-and-side-effects/treatment-types/radiation/basics.html>. Accessed 11.11.2022.
- [6] C. E. Olsson, A. Jackson, J. O. Deasy, and M. Thor, “A Systematic Post-QUANTEC Review of Tolerance Doses for Late Toxicity After Prostate Cancer Radiation Therapy,” *International journal of radiation oncology, biology, physics*, vol. 102(5), 2018, <https://doi.org/10.1016/j.ijrobp.2018.08.015>.
- [7] Siemens Healthineers, “Autocontouring in Radiation Therapy for Various Clinical Environments,” <https://www.siemens-healthineers.com/radiotherapy/software-solutions/autocontouring>. Access 25.04.2023.
- [8] Massachusetts Institute of Technology, “MIT researchers develop an AI model that can detect future lung cancer risk,” <https://news.mit.edu/2023/ai-model-can-detect-future-lung-cancer-0120>. Access 25.04.2023.
- [9] National Cancer Institute, “The Genetics of Cancer,” 2022, <https://www.cancer.gov/about-cancer/causes-prevention/genetics>. Accessed 16.02.2023.
- [10] —, “Cancer Staging,” 2022, <https://www.cancer.gov/about-cancer/diagnosis-staging/staging>. Accessed 13.02.2023.
- [11] American Association for Cancer Research, “About Cancer - What is Cancer ?” <https://www.aacr.org/patients-caregivers/about-cancer/what-is-cancer>. Accessed 03.02.2023.
- [12] National Cancer Institute, “Understanding Cancer - What is Cancer ?” <https://www.cancer.gov/about-cancer/understanding/what-is-cancer>. Accessed 23.05.2023.
- [13] American Cancer Society, “Treatment Types,” <https://www.cancer.org/cancer/managing-cancer/treatment-types.html>. Access 07.05.2023.

- [14] M. Bowser and J. Waxman, *"Lecture Notes: Oncology"*, 2nd ed. Wiley-Blackwell, 2010.
- [15] American Cancer Society, "How Is Chemotherapy Used to Treat Cancer?" <https://www.cancer.org/cancer/managing-cancer/treatment-types/chemotherapy/how-is-chemotherapy-used-to-treat-cancer.html>. Access 22.05.2023.
- [16] —, "Hormone Therapy," <https://www.cancer.org/cancer/managing-cancer/treatment-types/hormone-therapy.html>. Access 22.05.2023.
- [17] National Cancer Institute, "Cancer Treatment," <https://www.cancer.gov/about-cancer/treatment>. Access 22.05.2023.
- [18] A. Sibtain, A. Morgan, and N. MacDougall, *"Physics for Clinical Oncology"*, 1st ed. Oxford University Press, 2012.
- [19] National Cancer Institute, "Radiation Therapy to Treat Cancer," <https://www.cancer.gov/about-cancer/treatment/types/radiation-therapy>. Access 22.05.2023.
- [20] M. Schlachter, R. G. Raidou, L. P. Muren, B. Preim, P. M. Putora, and K. Bühler, "State-of-the-Art Report: Visual Computing in Radiation Therapy Planning," *Wiley Online Library*, 2019, <https://doi.org/10.1111/cgf.13726>.
- [21] Z. Xu, R. Yao, M. B. Podgorsak, and I. Z. Wang, "Effects of collimator angle, couch angle, and starting phase on motion-tracking dynamic conformal arc therapy (4D DCAT)," *Journal of Applied Clinical Medical Physics*, vol. 18, no. 5, pp. 54–63, 2017, <https://doi.org/10.1002/acm2.12132>.
- [22] American Society of Clinical Oncology, "What is Radiation Therapy?" <https://www.cancer.net/navigating-cancer-care/how-cancer-treated/radiation-therapy/what-radiation-therapy>. Access 25.04.2023.
- [23] National Cancer Institute, "External Beam Radiation Therapy for Cancer," <https://www.cancer.gov/about-cancer/treatment/types/radiation-therapy/external-beam>. Accessed 03.03.2023.
- [24] Physics World, "Finnish BNCT pioneers set their sights on clinical translation to the hospital campus," <https://physicsworld.com/a/finnish-bnct-pioneers-set-their-sights-on-clinical-translation-to-the-hospital-campus/>. Access 15.05.2023.
- [25] H. E. Romeijn, R. K. Ahuja, J. F. Dempsey, and A. Kumar, "A column generation approach to radiation therapy treatment planning using aperture modulation," *SIAM Journal on Optimization*, vol. 15, pp. 838–862, 01 2005, <https://doi.org/10.1137/040606612>.
- [26] International Atomic Energy Agency, "Definition of target volumes and organs at risk," https://humanhealth.iaea.org/HHW/RadiationOncology/Treatingpatients/Treatment_planning_and_techniques/Training_Course/12_Defining_target_volumes_and_organs_at_risk.pdf. Access 05.03.2023.

- [27] J. S. Ballard, "*Radiation Safety*". Open Oregon Educational Resources, 2020.
- [28] P. Shirley, M. Ashikhmin, and S. Marschner, "*Fundamentals of Computer Graphics*", 3rd ed. CRC Press, 2009.
- [29] J. Lehtinen, "Lecture 1: Overview, Lecture 2: Transformations, and Lecture 11: Introduction to Rendering and Ray Tracing," 2021, CS-C3100 - Computer Graphics, Aalto University.
- [30] Stanford University Computer Graphics Laboratory, "The Stanford 3D Scanning Repository," <https://graphics.stanford.edu/data/3Dscanrep/>. Access 23.05.2023.
- [31] Blender, "Introduction," <https://docs.blender.org/manual/de/2.79/render/introduction.html>. Access 23.05.2023.
- [32] H.-C. Chua, "3D Graphics with OpenGL Basic Theory," https://www3.ntu.edu.sg/home/ehchua/programming/opengl/CG_BasicsTheory.html. Access 23.05.2023.
- [33] MDN Web Docs, "Coordinate systems," https://developer.mozilla.org/en-US/docs/Web/CSS/CSSOM_View/Coordinate_systems. Access 23.05.2023.
- [34] B. Caulfield, "What Is Path Tracing?" <https://blogs.nvidia.com/blog/2022/03/23/what-is-path-tracing/>. Access 15.05.2023.
- [35] J. Kajiya, "The rendering equation," <https://doi.org/10.1145/15886.15902>. Access 15.05.2023.
- [36] A. S. Glassner, Ed., "*An Introduction to Ray Tracing*". GBR: Academic Press Ltd., 1989.
- [37] G. R. Hofmann, "Who invented ray tracing?" *The Visual Computer*, vol. 6, 1990, <https://doi.org/10.1007/BF01911003>.
- [38] A. Appel, "Some techniques for shading machine renderings of solids," *Spring Joint Computer Conference*, 1968, <https://doi.org/10.1145/1468075.1468082>.
- [39] I. Goodfellow, Y. Bengio, and A. Courville, "*Deep Learning*". MIT Press, 2016, <http://www.deeplearningbook.org>. Accessed 11.11.2022.
- [40] A. Turing, "Computing Machinery and Intelligence," *Mind*, vol. LIX, no. 236, pp. 433–460, 10 1950, <https://doi.org/10.1093/mind/LIX.236.433>.
- [41] MIT Museum, "Theseus," <https://mitmuseum.mit.edu/collections/object/2007.030.001>. Access 17.05.2023.
- [42] A. L. Samuel, "Some studies in machine learning using the game of checkers," *IBM Journal of Research and Development*, vol. 44, no. 1.2, pp. 206–226, 2000, <https://doi.org/10.1147/rd.441.0206>.
- [43] T. M. Mitchell, "*Machine Learning*". McGraw-Hill, 1997.

- [44] C. Bishop, *"Pattern Recognition and Machine Learning"*. Springer, 2006.
- [45] J. Rousu, "Lecture 1: Introduction," 2020, CS-E4710 Machine Learning: Supervised Methods, Aalto University.
- [46] S. Lloyd, "Least squares quantization in PCM," *IEEE Transactions on Information Theory*, vol. 28, no. 2, pp. 129–137, 1982, <https://doi.org/10.1109/TIT.1982.1056489>.
- [47] Google, "k-Means Advantages and Disadvantages," <https://developers.google.com/machine-learning/clustering/algorithm/advantages-disadvantages>. Access 22.05.2023.
- [48] F. Pedregosa, G. Varoquaux, A. Gramfort *et al.*, "Scikit-learn: Machine learning in Python," *Journal of Machine Learning Research*, vol. 12, pp. 2825–2830, 2011.
- [49] P. J. Rousseeuw, "Silhouettes: A graphical aid to the interpretation and validation of cluster analysis," *Journal of Computational and Applied Mathematics*, vol. 20, pp. 53–65, 1987, [https://doi.org/10.1016/0377-0427\(87\)90125-7](https://doi.org/10.1016/0377-0427(87)90125-7).
- [50] W. Hämmäläinen, "Clustering validation," 2020, CS-E4650 - Methods of Data Mining, Aalto University.
- [51] D. L. Davies and D. W. Bouldin, "A cluster separation measure," *IEEE Transactions on Pattern Analysis and Machine Intelligence*, vol. PAMI-1, no. 2, pp. 224–227, 1979, <https://doi.org/10.1109/TPAMI.1979.4766909>.
- [52] UC Health, "Lung Cancer," <https://www.uchealth.com/en/conditions/lung-cancer>. Access 06.05.2023.
- [53] International Atomic Energy Agency, "Chapter 11: Computed Tomography," https://humanhealth.iaea.org/HHW/MedicalPhysics/TheMedicalPhysicist/Studentscorner/HandbookforTeachersandStudents/Chapter_11.pdf. Access 02.05.2023.
- [54] M.-H. Li, S.-F. Huang, C.-C. Chang *et al.*, "Variations in dosimetric distribution and plan complexity with collimator angles in hypofractionated volumetric arc radiotherapy for treating prostate cancer." *Journal of Applied Clinical Medical Physics*, vol. 19, no. 2, pp. 93–102, 2018, <https://doi.org/10.1002/acm2.12249>.
- [55] S. McDowell, "Study: Young Women Now Have Higher Rates for Lung Cancer Than Men Worldwide," 2020, <https://www.cancer.org/research/acs-research-news/study-young-women-now-have-higher-rate-for-lung-cancer-than-men-worldwide.html>. Access 06.05.2023.
- [56] I. Baiu, A. L. Titan, L. W. Martin *et al.*, "The role of gender in non-small cell lung cancer: a narrative review." *Journal of thoracic disease*, vol. 13, no. 6, pp. 3816–3826, 2021, <https://doi.org/10.21037/jtd-20-3128>.

- [57] J. Pinto, C. S. Vallejos, L. E. Raez *et al.*, “Gender and outcomes in non-small cell lung cancer: an old prognostic variable comes back for targeted therapy and immunotherapy?” *ESMO open*, vol. 3, no. 3, 2018, <https://doi.org/10.1136/esmoopen-2018-000344>.
- [58] S. Webb, “*Contemporary IMRT: Developing Physics and Clinical Implementation*”. IOP Publishing Ltd, 2005.

Alphabetical Index

Symbols			
3D-CRT	17		
A		I	
API	26	Imbalanced data	33
C		IMRT	9, 17
Camera space	27	Initial consultation	24
Cancer	12	Irradiated Volume	20
Carcinomas	14	ITV	20
Chemo	14	K	
Chemotherapy	14	K-means	35
Cityblock distance	36	L	
CNS cancers	14	L1 distance	36
Computer graphics	25	Leukemias	14
Confusion matrix	34	LINAC	16
Cosine similarity	35	Lymphomas	14
CT	17	M	
CTV	20	Manhattan distance	36
D		Medical dosimetrist	24
Davies–Bouldin index	37	Medical physicist	24
DICOM	15	Monitor Unit	21
Dose distribution	22	MRI	17
E		N	
Edges	26	Neutron	19
Electrons	19	Noisy data	33
Endocrine therapy	15	O	
Euclidean distance	36	OAR	10
F		Object space	27
Faces	26	Overfitting	33
G		P	
GPU	26	Photons	18
Graphics pipeline	26	Planar perspective transformation	28
Great circle distance	35	Post-treatment follow-up	25
GTV	20	Projective transformation	28
H		Protons	18
Haversine distance	35	PTV	20
Homogeneous coordinates	29	R	
Hormone therapy	15	Radiation oncologist	24
		Radiation oncology nurse	25
		Radiotherapy	15
		Reflection	27
		Reinforcement learning	33

RMSE	33		
Rotation	27		
RTDOSE	42		
RTPLAN	42		
RTSTRUCT	38		
		S	
Sarcomas	14		
SBRT	17		
Scaling	27		
Screen space	27		
Shearing	27		
Silhouette index	36		
Simulation	24		
SRS	17		
SRT	17		
SSD	22		
SSE	35		
Supervised learning	32		
Surgery	14		
			T
		TNM	12
		Translation	27
		Treated Volume	20
		Treatment delivery	24
		Treatment planning	24
		Triangle mesh	26
			U
		Underfitting	33
		Unsupervised learning	32
			V
		Vertices	26
		Viewing pipeline	26
		VMAT	17
			W
		World space	27

A Angle discovery performance

Patient	No. CT slices	No. OARs	Fusion time (s)	Color cal. time (s)
LUNG1-001	21	3	7.27	1.56
LUNG1-002	26	5	10.44	1.36
LUNG1-003	17	5	7.23	1.73
LUNG1-004	36	4	14.31	1.49
LUNG1-005	24	5	13.31	1.50
LUNG1-006	23	5	9.22	1.70
LUNG1-007	10	5	3.93	1.48
LUNG1-008	15	5	5.30	1.55
LUNG1-009	22	4	9.13	1.72
LUNG1-010	13	5	4.78	1.55
LUNG1-011	14	5	4.92	1.82
LUNG1-012	29	5	13.42	1.73
LUNG1-013	8	3	4.24	1.59
LUNG1-014	11	5	3.58	1.43
LUNG1-015	5	3	1.54	1.45
LUNG1-016	22	5	9.32	1.60
LUNG1-017	43	4	21.05	1.51
LUNG1-018	24	4	9.30	1.41
LUNG1-019	19	4	8.46	1.87
LUNG1-020	19	5	11.51	1.35
LUNG1-021	29	5	11.80	1.36
LUNG1-022	27	5	13.55	1.48
LUNG1-023	36	5	15.63	1.64
LUNG1-024	13	5	4.43	1.75
LUNG1-025	24	5	9.56	1.41
LUNG1-026	48	5	20.38	1.64
LUNG1-027	3	3	0.91	1.74
LUNG1-028	14	5	5.23	1.36
LUNG1-029	15	3	4.50	1.37
LUNG1-030	27	5	14.16	1.54
LUNG1-031	18	5	6.83	1.41
LUNG1-032	27	4	10.40	1.28
LUNG1-033	30	5	13.09	1.55
LUNG1-034	23	5	8.28	1.48
LUNG1-036	15	3	4.40	1.28
LUNG1-037	9	4	3.27	1.40
LUNG1-038	26	5	10.07	1.46
LUNG1-039	9	5	3.24	1.62
LUNG1-040	22	5	7.74	1.84
LUNG1-041	15	4	4.72	1.34

LUNG1-042	28	5	15.93	1.55
LUNG1-043	44	5	18.54	1.50
LUNG1-044	27	4	9.78	1.51
LUNG1-045	16	3	5.27	1.54
LUNG1-046	23	5	11.17	1.45
LUNG1-047	27	4	10.67	1.70
LUNG1-048	19	3	11.60	1.29
LUNG1-049	4	3	1.48	1.57
LUNG1-051	17	5	6.77	1.38
LUNG1-052	22	4	8.76	1.53

B Angle discovery result

Angle	Left lung cancer	Right lung cancer	Bilateral cancer
0	0.18	0.28	0.04
1	0.20	0.30	0.06
2	0.20	0.30	0.06
3	0.20	0.28	0.06
4	0.18	0.28	0.06
5	0.20	0.28	0.06
6	0.18	0.28	0.06
7	0.18	0.28	0.08
8	0.18	0.26	0.08
9	0.16	0.26	0.08
10	0.18	0.26	0.08
11	0.18	0.26	0.08
12	0.18	0.26	0.06
13	0.22	0.24	0.04
14	0.22	0.26	0.04
15	0.22	0.26	0.04
16	0.24	0.26	0.02
17	0.24	0.26	0.02
18	0.22	0.24	0.02
19	0.22	0.24	0.02
20	0.22	0.26	0.02
21	0.22	0.22	0.02
22	0.22	0.22	0.02
23	0.22	0.22	0.02
24	0.22	0.22	0.02
25	0.22	0.22	0.02
26	0.24	0.24	0.02
27	0.24	0.28	0.02
28	0.24	0.26	0.02
29	0.24	0.26	0.02
30	0.24	0.28	0.02
31	0.24	0.22	0.02
32	0.24	0.26	0.02
33	0.24	0.20	0.02
34	0.24	0.20	0.02
35	0.24	0.16	0.02
36	0.22	0.14	0.02
37	0.22	0.16	0.00
38	0.22	0.14	0.00
39	0.24	0.14	0.00

40	0.24	0.18	0.00
41	0.24	0.16	0.00
42	0.24	0.12	0.00
43	0.24	0.12	0.00
44	0.22	0.10	0.00
45	0.24	0.10	0.00
46	0.24	0.08	0.00
47	0.24	0.06	0.00
48	0.24	0.06	0.00
49	0.24	0.06	0.00
50	0.24	0.06	0.00
51	0.24	0.06	0.00
52	0.24	0.06	0.00
53	0.24	0.06	0.00
54	0.24	0.06	0.00
55	0.24	0.04	0.00
56	0.24	0.02	0.00
57	0.24	0.02	0.00
58	0.24	0.04	0.00
59	0.24	0.04	0.00
60	0.24	0.04	0.00
61	0.24	0.04	0.00
62	0.24	0.04	0.00
63	0.24	0.02	0.00
64	0.26	0.02	0.00
65	0.24	0.02	0.00
66	0.26	0.02	0.00
67	0.26	0.02	0.00
68	0.26	0.02	0.00
69	0.26	0.02	0.00
70	0.26	0.02	0.00
71	0.26	0.02	0.00
72	0.26	0.02	0.00
73	0.24	0.02	0.00
74	0.26	0.02	0.00
75	0.26	0.02	0.00
76	0.26	0.02	0.00
77	0.26	0.00	0.00
78	0.26	0.00	0.00
79	0.24	0.00	0.00
80	0.24	0.00	0.00
81	0.20	0.00	0.00
82	0.20	0.00	0.00

83	0.20	0.00	0.00
84	0.20	0.00	0.00
85	0.22	0.00	0.00
86	0.26	0.00	0.00
87	0.22	0.00	0.00
88	0.20	0.00	0.00
89	0.24	0.00	0.00
90	0.22	0.00	0.00
91	0.22	0.00	0.00
92	0.22	0.00	0.00
93	0.22	0.00	0.00
94	0.22	0.00	0.00
95	0.22	0.00	0.00
96	0.22	0.00	0.00
97	0.20	0.00	0.00
98	0.20	0.00	0.00
99	0.22	0.00	0.00
100	0.22	0.00	0.00
101	0.20	0.00	0.00
102	0.22	0.00	0.00
103	0.22	0.00	0.00
104	0.22	0.00	0.00
105	0.20	0.04	0.00
106	0.22	0.06	0.00
107	0.22	0.08	0.00
108	0.22	0.10	0.00
109	0.22	0.12	0.00
110	0.22	0.12	0.00
111	0.22	0.12	0.00
112	0.24	0.12	0.00
113	0.22	0.14	0.00
114	0.24	0.16	0.00
115	0.22	0.16	0.00
116	0.22	0.18	0.00
117	0.22	0.20	0.00
118	0.22	0.20	0.00
119	0.24	0.18	0.00
120	0.24	0.20	0.00
121	0.24	0.18	0.00
122	0.24	0.18	0.00
123	0.24	0.18	0.00
124	0.24	0.22	0.00
125	0.24	0.22	0.02

126	0.24	0.28	0.02
127	0.24	0.32	0.04
128	0.24	0.32	0.04
129	0.24	0.32	0.04
130	0.24	0.36	0.04
131	0.26	0.34	0.02
132	0.26	0.36	0.02
133	0.26	0.30	0.02
134	0.26	0.32	0.02
135	0.26	0.32	0.02
136	0.26	0.30	0.02
137	0.26	0.34	0.02
138	0.28	0.36	0.02
139	0.28	0.38	0.02
140	0.28	0.38	0.02
141	0.28	0.40	0.02
142	0.28	0.40	0.02
143	0.28	0.40	0.04
144	0.26	0.38	0.04
145	0.26	0.36	0.04
146	0.26	0.36	0.04
147	0.26	0.38	0.04
148	0.26	0.34	0.04
149	0.24	0.36	0.04
150	0.24	0.34	0.04
151	0.26	0.36	0.04
152	0.26	0.40	0.04
153	0.26	0.42	0.06
154	0.26	0.42	0.04
155	0.26	0.42	0.04
156	0.26	0.42	0.04
157	0.26	0.44	0.04
158	0.26	0.42	0.06
159	0.24	0.42	0.04
160	0.26	0.42	0.04
161	0.26	0.42	0.04
162	0.22	0.42	0.04
163	0.26	0.42	0.04
164	0.22	0.42	0.06
165	0.24	0.44	0.04
166	0.26	0.44	0.04
167	0.24	0.44	0.04
168	0.24	0.42	0.06

169	0.24	0.42	0.06
170	0.26	0.42	0.06
171	0.24	0.42	0.06
172	0.24	0.42	0.06
173	0.24	0.42	0.06
174	0.24	0.44	0.06
175	0.24	0.44	0.06
176	0.22	0.40	0.06
177	0.22	0.46	0.06
178	0.24	0.42	0.06
179	0.22	0.42	0.04
180	0.22	0.42	0.06
181	0.22	0.44	0.04
182	0.22	0.40	0.04
183	0.20	0.38	0.04
184	0.22	0.42	0.04
185	0.24	0.42	0.04
186	0.24	0.40	0.04
187	0.26	0.42	0.04
188	0.26	0.40	0.04
189	0.26	0.40	0.04
190	0.26	0.42	0.04
191	0.24	0.38	0.04
192	0.26	0.42	0.04
193	0.26	0.42	0.04
194	0.26	0.40	0.04
195	0.26	0.40	0.04
196	0.26	0.44	0.04
197	0.26	0.44	0.04
198	0.26	0.42	0.04
199	0.28	0.46	0.04
200	0.28	0.42	0.04
201	0.28	0.44	0.04
202	0.24	0.44	0.04
203	0.24	0.42	0.04
204	0.24	0.44	0.04
205	0.24	0.44	0.04
206	0.22	0.44	0.04
207	0.24	0.46	0.04
208	0.24	0.44	0.04
209	0.22	0.44	0.04
210	0.22	0.44	0.04
211	0.22	0.42	0.04

212	0.22	0.46	0.04
213	0.22	0.46	0.04
214	0.18	0.48	0.04
215	0.20	0.50	0.04
216	0.20	0.50	0.02
217	0.18	0.50	0.04
218	0.18	0.50	0.04
219	0.18	0.48	0.02
220	0.20	0.50	0.02
221	0.20	0.48	0.02
222	0.20	0.52	0.02
223	0.20	0.48	0.02
224	0.18	0.50	0.02
225	0.20	0.48	0.02
226	0.22	0.48	0.02
227	0.22	0.46	0.02
228	0.20	0.48	0.02
229	0.22	0.46	0.02
230	0.20	0.48	0.00
231	0.18	0.46	0.00
232	0.14	0.44	0.00
233	0.16	0.44	0.02
234	0.16	0.44	0.02
235	0.16	0.44	0.02
236	0.16	0.44	0.02
237	0.14	0.44	0.00
238	0.14	0.44	0.00
239	0.10	0.44	0.00
240	0.10	0.42	0.00
241	0.10	0.42	0.00
242	0.10	0.38	0.00
243	0.10	0.38	0.00
244	0.12	0.38	0.00
245	0.10	0.36	0.00
246	0.10	0.36	0.00
247	0.08	0.36	0.00
248	0.08	0.36	0.00
249	0.08	0.38	0.00
250	0.08	0.36	0.00
251	0.08	0.36	0.00
252	0.08	0.38	0.00
253	0.06	0.38	0.00
254	0.06	0.38	0.00

255	0.02	0.38	0.00
256	0.02	0.38	0.00
257	0.02	0.38	0.00
258	0.02	0.38	0.00
259	0.02	0.36	0.00
260	0.02	0.36	0.00
261	0.02	0.36	0.00
262	0.00	0.36	0.00
263	0.00	0.34	0.00
264	0.00	0.36	0.00
265	0.00	0.36	0.00
266	0.00	0.32	0.00
267	0.00	0.34	0.00
268	0.00	0.36	0.00
269	0.00	0.36	0.00
270	0.00	0.34	0.00
271	0.00	0.36	0.00
272	0.00	0.38	0.00
273	0.00	0.40	0.00
274	0.00	0.40	0.00
275	0.00	0.40	0.00
276	0.00	0.42	0.00
277	0.00	0.42	0.00
278	0.00	0.40	0.00
279	0.00	0.44	0.00
280	0.00	0.42	0.00
281	0.00	0.48	0.02
282	0.00	0.44	0.02
283	0.00	0.44	0.02
284	0.00	0.44	0.02
285	0.00	0.44	0.02
286	0.00	0.44	0.02
287	0.00	0.46	0.02
288	0.00	0.44	0.02
289	0.00	0.46	0.02
290	0.00	0.46	0.02
291	0.02	0.44	0.02
292	0.02	0.44	0.02
293	0.02	0.46	0.02
294	0.02	0.42	0.02
295	0.02	0.40	0.02
296	0.02	0.40	0.02
297	0.02	0.42	0.02

298	0.00	0.40	0.02
299	0.00	0.42	0.02
300	0.04	0.38	0.02
301	0.04	0.44	0.02
302	0.04	0.42	0.00
303	0.04	0.42	0.00
304	0.04	0.36	0.00
305	0.04	0.38	0.00
306	0.04	0.38	0.00
307	0.04	0.36	0.00
308	0.04	0.36	0.00
309	0.04	0.36	0.02
310	0.04	0.40	0.02
311	0.06	0.34	0.02
312	0.06	0.36	0.02
313	0.06	0.36	0.02
314	0.06	0.38	0.02
315	0.08	0.30	0.02
316	0.06	0.34	0.00
317	0.06	0.30	0.02
318	0.08	0.36	0.00
319	0.08	0.32	0.00
320	0.08	0.34	0.00
321	0.08	0.34	0.00
322	0.06	0.30	0.00
323	0.06	0.32	0.00
324	0.08	0.32	0.00
325	0.08	0.34	0.02
326	0.10	0.32	0.02
327	0.10	0.32	0.02
328	0.10	0.34	0.02
329	0.10	0.36	0.02
330	0.10	0.32	0.02
331	0.10	0.32	0.02
332	0.10	0.32	0.02
333	0.10	0.36	0.02
334	0.10	0.32	0.02
335	0.10	0.32	0.02
336	0.12	0.32	0.02
337	0.12	0.32	0.02
338	0.10	0.32	0.02
339	0.10	0.30	0.02
340	0.12	0.28	0.02

341	0.14	0.30	0.02
342	0.12	0.28	0.02
343	0.14	0.28	0.02
344	0.18	0.28	0.02
345	0.16	0.28	0.02
346	0.16	0.28	0.02
347	0.16	0.28	0.02
348	0.14	0.30	0.02
349	0.14	0.28	0.02
350	0.14	0.28	0.02
351	0.14	0.30	0.02
352	0.14	0.32	0.02
353	0.16	0.30	0.04
354	0.18	0.32	0.04
355	0.18	0.30	0.04
356	0.18	0.30	0.04
357	0.18	0.30	0.04
358	0.18	0.28	0.04
359	0.18	0.30	0.06